

# Analysis Notes: Underlying-event Activity Measurement in p+p Collisions at 200 GeV

Helen Caines, Li Yi, Kevin Adkins, David Stewart

April 20, 2018

## Contents

<b>1</b>	<b>Introduction and Overview</b>	<b>2</b>
<b>2</b>	<b>Experiment Data Selection</b>	<b>2</b>
<b>3</b>	<b>Jet Reconstructions</b>	<b>8</b>
<b>4</b>	<b>Simulation</b>	<b>9</b>
<b>5</b>	<b>Method</b>	<b>12</b>
<b>6</b>	<b>Trigger Bias Correction</b>	<b>14</b>
<b>7</b>	<b>Unfold Detector Effect</b>	<b>18</b>
7.1	Unfolded Distributions . . . . .	20
7.2	Closure Test . . . . .	22
<b>8</b>	<b>Pile-up</b>	<b>23</b>
<b>9</b>	<b>Results</b>	<b>24</b>
<b>10</b>	<b>Systematical Uncertainty</b>	<b>27</b>
<b>11</b>	<b>Discussion</b>	<b>34</b>
11.1	TransMax Vs TransMin . . . . .	34
11.2	Energy Dependence . . . . .	35
11.3	Leading Charged Particle . . . . .	37
11.4	JP0, JP1, JP2 . . . . .	39
11.5	Dijet . . . . .	40
11.6	Unfolding Prior . . . . .	41
<b>12</b>	<b>Location of Computing Code</b>	<b>44</b>
<b>13</b>	<b>Conclusion</b>	<b>45</b>

# 1 Introduction and Overview

In proton+proton (p+p) collisions, when a hard scattering happens, there could be multiple processes happen on top of the primary hard scattering. Those multiple processes are experimentally referred as underlying-event activity. Hard scattering is parton-parton scattering with large momentum transferred from longitudinal to transverse plane. Underlying-event activity includes second or multiple parton interactions (MPI), the gluon radiations and quark-antiquark splitting from the initial or final state partons of the primary hard scattering (ISR/FSR), the color reconnections with the beam direction remanent partons (BRR). The partons produced in those processes reduce their virtuality and finally fragmented into mostly lower energy soft hadrons. Hard physics can be calculated by pQCD and there is a good agreement between experiment measurements and theoretical calculations [1, 2]. Soft physics, which dominated underlying-event activity, faces the non-factorization and non-perturbation calculation challenging. Study of underlying-event activity, which gives the relationship between soft physics and hard physics, can help us to understand QCD process and theoretical modeling.

Underlying-event activity is experimentally accessed through topological structure observable: particle productions away from the primary hard scattering directions. CDF collaboration used the highest transverse momentum  $p_T$  charged particle, leading jet, or Drell-Yan pair in each proton+antiproton event for hard scattering direction [3, 4]. At LHC energies, ALICE, ATLAS, CMS collaborations had used highest  $p_T$  charged particle, charged jet, full jet, or  $Z$  boson as hard scattering references [5, 6, 7, 8, 9]. In this analysis, we used the fully reconstructed jet as hard scattering reference.

At TeV collision energy scale, particle productions sensitive to underlying-event activity at mid-rapidity were observed to be positively correlated with observable sensitive to hard scattering energy at mid-rapidity [4, 5, 6, 7, 8, 9]. Underlying-event particle productions at forward rapidity relationships with leading jet  $p_T$  were however observed to be collision energy depended by CMS collaboration [10]: at  $\sqrt{s_{NN}} = 0.9$  TeV, they were negatively correlated; at 7 TeV, they were mostly positively correlated at leading charge jet  $1 \text{ GeV}/c < p_T < 15 \text{ GeV}/c$ . The negatively correlations at lower energy could be due to that the total energy conservation has larger constrain with similar order of hard scatterings. At RHIC energy, total energy conservation may have larger constrain at similar order of hard scatterings than that in TeV scale collisions.

In this analysis, we measured underlying-event activity in proton+proton collisions at  $\sqrt{s_{NN}} = 200$  GeV by STAR experiment at RHIC.

## 2 Experiment Data Selection

0.16 billion Jet Patch (JP) and 0.6 billion Minimum-Bias (MB) p+p collisions at  $\sqrt{s_{NN}} = 200$  GeV from year 2012 were used. Production P12id. JP trigger had no requirement in VPD. MB trigger had east and west VPD coincidence requirement (VPD<sub>MB-nosmd</sub>). 3 JP triggers were used in Run12. Their transverse energy thresholds are 3.5 GeV for JP0 (with DSM threshold 20), 5.4 GeV for JP1 (DSM 28), 7.3 GeV for JP2 (DSM 36). (trigger setup for run12: <http://www.star.bnl.gov/protected/common/common2012/trigger2012/triggers2012.html>) The average prescale for those triggers are 110.52 for MB, 141.35 for JP0, 2.5 for JP1, 1 for JP2. The efficiencies of JP triggers from embedding (Section 4) are shown in Fig. 1.

The reconstructed tracks in Time Projection Chamber (TPC) and deposit energy in Barrel Electromagnetic Calorimeter (BEMC) are used in this analysis.

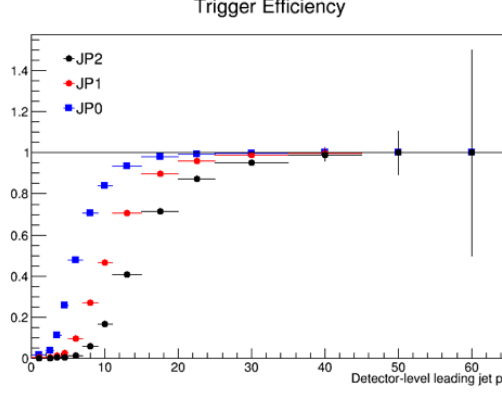


Figure 1: Jet patch trigger efficiencies from embedding. The x-axis is the detector-level reconstructed leading jet  $p_T$ .

- The highest ranking vertex with ranking cut  $> 0$  is selected for each event. The events primary vertex position on  $z$  direction (beam direction) are required to be within  $|z_{vtx}| < 30$  cm from the TPC center.
- The events contained any primary charged particle with  $p_T > 20$  GeV/ $c$  or deposit neutral energy  $E_T > 20$  GeV were discarded to avoid events with low tracking reconstruction resolution or hot tower in BEMC. The fraction of primary charged particle with measured  $p_T > 20$  GeV/ $c$  is less than  $3e-5$ . BEMC tower ones are dominated by hot tower which is discussed later.
- BEMC tower energy is corrected by 100% hadronic correction to avoid double counting of charged particle energy .
- BEMC towers with energy less than 0.2 GeV were discarded.

TPC track cuts are listed in Table 1.

Sample QA plots:

Beside the cuts above, we also check the time dependence of each variable for any abnormal jump. For example, Fig. 2 shows there is a deviation of Vz distribution around day 47 and those runs are removed.

The run numbers of removed run: 13040003, 13040016, 13040017, 13040018, 13040037, 13040040, 13040041, 13040042, 13040043, 13040044, 13040045, 13040046, 13041002, 13041004, 13041006,

Table 1: Primary Track Quality Cuts

---

$ \eta  < 1$
Hits points for TPC tracks $\geq 20$
Hits points/possible hits point $\geq 0.52$
global $dca < 1$ cm
$0.2 < p_T < 20$ GeV/ $c$

---

13041007, 13041008, 13041009, 13041010, 13041082, 13041101, 13041102, 13041108, 13041109, 13041110, 13041115, 13041116, 13041119, 13042001, 13042002, 13042003, 13042006, 13042007, 13042008, 13042013, 13042015, 13042016, 13042017, 13042018, 13042019, 13042020, 13042022, 13042023, 13042024, 13042025, 13042026, 13042027, 13042046, 13042047, 13042048, 13042049, 13042050, 13043005, 13043006, 13043011, 13043012, 13043013, 13043017, 13043023, 13043030, 13043031, 13043032, 13043035, 13043044, 13043047, 13043048, 13043049, 13043050, 13043051, 13043052, 13043053, 13043054, 13043055, 13043056, 13043057, 13043058, 13043059, 13043060, 13043063, 13044017, 13044018, 13044019, 13044020, 13044021, 13044022, 13044023, 13044024, 13044025, 13044026, 13044029, 13044030, 13044031, 13044034, 13044118, 13044119, 13044121, 13044122, 13044123, 13044124, 13044125, 13044126, 13045001, 13045003, 13045005, 13045006, 13045007, 13045012, 13045029, 13045056, 13045133, 13045134, 13045135, 13045138, 13045145, 13045146, 13045164, 13046001, 13046002, 13046003, 13046004, 13046008, 13046010, 13046011, 13046012, 13046013, 13046014, 13046015, 13046017, 13046028, 13046029, 13046118, 13046119, 13046120, 13046121, 13047002, 13047003, 13047004, 13047014, 13047018, 13047022, 13047023, 13047024, 13047026, 13047027, 13047028, 13047029, 13047030, 13047031, 13047032, 13047033, 13047034, 13047035, 13047036, 13047037, 13047039, 13047040, 13047041, 13047042, 13047043, 13047044, 13047045, 13047046, 13047047, 13047048, 13047049, 13047050, 13047051, 13047052, 13047053, 13047054, 13047055, 13047122, 13047123, 13047124, 13047126, 13048007, 13048022, 13048046, 13049004, 13049005, 13049050, 13049052, 13049075, 13049086, 13049087, 13049088, 13049089, 13050007, 13050025, 13050026, 13050027, 13050033, 13050039, 13050042, 13050043, 13050044, 13050046, 13050047, 13050049, 13050050, 13051068, 13051080, 13051088, 13051095, 13051102, 13052021, 13052022, 13052054, 13052063, 13052068, 13053010, 13053021, 13054004, 13054005, 13054006, 13054007, 13054008, 13054009, 13054011, 13054012, 13054013, 13054014, 13054015, 13054016, 13054017, 13054018, 13054019, 13054020, 13054022, 13054042, 13054045, 13054046, 13054057, 13055015, 13055072, 13055081, 13055082, 13055086, 13055087, 13055088, 13055089, 13055090, 13056011, 13056012, 13056034, 13056035, 13056037, 13056038, 13056039, 13057038, 13057039, 13058019, 13058030, 13058047, 13058048, 13059003, 13059004, 13059005, 13059006, 13059007, 13059008, 13059009, 13059010, 13059011, 13059012, 13059013, 13059014, 13059015, 13059016, 13059017, 13059018, 13059019, 13059020, 13059021, 13059022, 13059023, 13059025, 13059026, 13059027, 13059035, 13059037, 13059038, 13059039, 13059076, 13059077, 13059078, 13059079, 13059080, 13059082, 13059083, 13059084, 13059085, 13059086, 13059087, 13060001, 13060002, 13060003, 13060009, 13060012, 13061026, 13063033, 13064030, 13064057, 13064059, 13064074, 13065048, 13066035, 13066036, 13066101, 13066102, 13066104, 13066109, 13066110, 13067001, 13067002, 13067003, 13067004, 13067005, 13067006, 13067007, 13067008, 13067009, 13067010, 13067011, 13067012, 13067013, 13067014, 13067015, 13067017, 13068017, 13068022, 13068027, 13068029, 13068034, 13068036, 13068037, 13069006, 13069009, 13069029, 13070030, 13070056, 13071034, 13071037, 13071038, 13071040.

BEMC towers with abnormal energy distributions were removed. The hot tower could appear

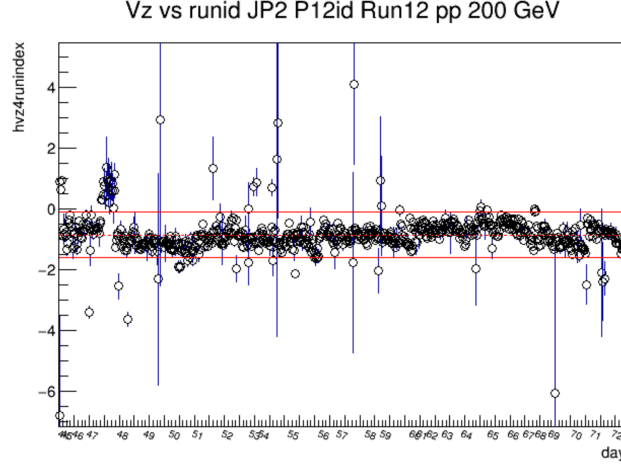


Figure 2: Mean TPC  $V_z$  as a function of runing days. Each point is for one run.

only at certain energy range. Therefore when checking for hot tower, one needs to look at various energy ranges. For example, tower 3407 shown in Figure 3 has similar energy spectrum as the normal tower for the majority of the energy range, but it has abnormal high frequency around 30 GeV/c. If one only check the frequency for this tower with energy  $> 2$  GeV/c for example, this tower will be missed from hot tower list. Figure 4 shows examples from JP2 and MB BEMC tower energy spectra before (blue) and after (red) bad tower removal.

Questionable tower id: 34, 106, 113, 160, 266, 267, 275, 280, 282, 286, 287, 293, 360, 410, 493, 504, 533, 541, 555, 561, 562, 594, 615, 616, 629, 633, 637, 638, 647, 650, 653, 657, 671, 673, 743, 779, 789, 790, 791, 792, 806, 809, 810, 811, 812, 813, 814, 821, 822, 823, 824, 829, 830, 831, 832, 837, 841, 842, 843, 844, 846, 849, 850, 851, 852, 857, 875, 897, 899, 903, 939, 953, 954, 956, 993, 1026, 1046, 1048, 1080, 1081, 1100, 1125, 1130, 1132, 1180, 1197, 1198, 1199, 1200, 1207, 1217, 1218, 1219, 1220, 1221, 1222, 1223, 1224, 1237, 1238, 1240, 1241, 1242, 1243, 1244, 1257, 1258, 1259, 1260, 1284, 1306, 1312, 1337, 1348, 1353, 1354, 1388, 1407, 1409, 1434, 1438, 1448, 1537, 1567, 1574, 1597, 1612, 1654, 1668, 1709, 1713, 1762, 1765, 1766, 1877, 1878, 1984, 2027, 2032, 2043, 2054, 2073, 2077, 2092, 2093, 2097, 2107, 2162, 2168, 2214, 2305, 2392, 2409, 2415, 2439, 2445, 2459, 2589, 2590, 2633, 2652, 2749, 2834, 2961, 2969, 3005, 3017, 3070, 3071, 3186, 3220, 3289, 3360, 3407, 3493, 3494, 3495, 3508, 3588, 3604, 3611, 3668, 3678, 3679, 3690, 3692, 3720, 3732, 3738, 3838, 3840, 3927, 3945, 4005, 4006, 4013, 4018, 4019, 4053, 4059, 4124, 4217, 4288, 4331, 4355, 4357, 4458, 4464, 4500, 4677, 4678, 4684, 4768

After BEMC tower removal, we still find there is a hot stripe for jet distribution in early runs of MB trigger and those runs (runid<13046029) are also removed, see Fig. 5. Those runs also have abnormal distributions from the rest in other variables, such as low BBC, ZDC coincidence rates, low mean DCA and so on.

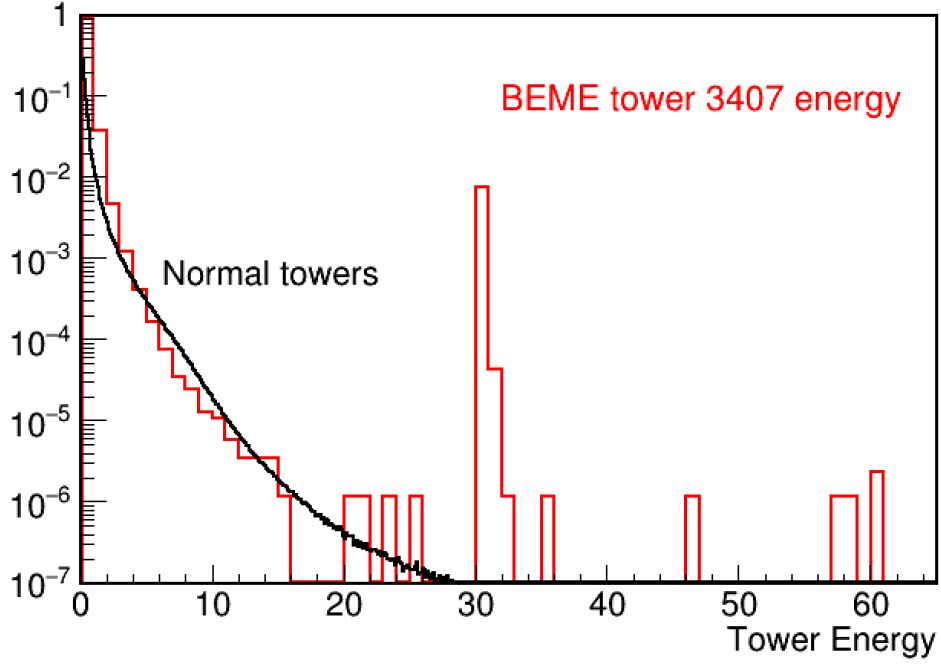


Figure 3: Energy spectrum for tower 3407.

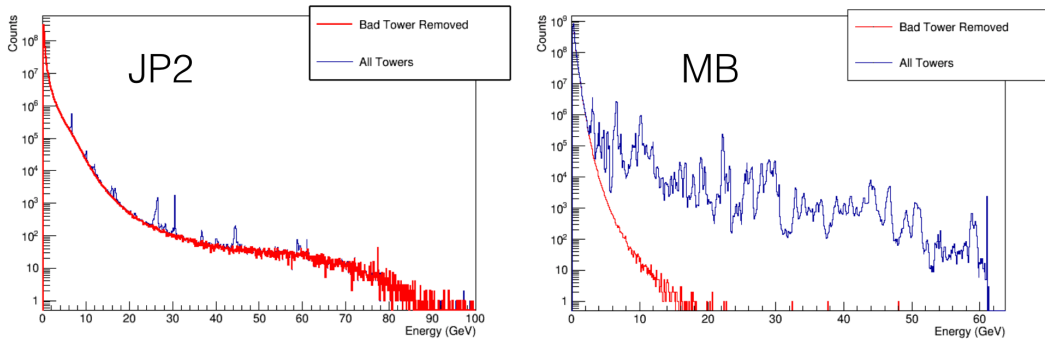


Figure 4: Before (blue) and after (red) bad tower removal for BEMC tower spectra of JP2 (left) and MB (right) triggers.

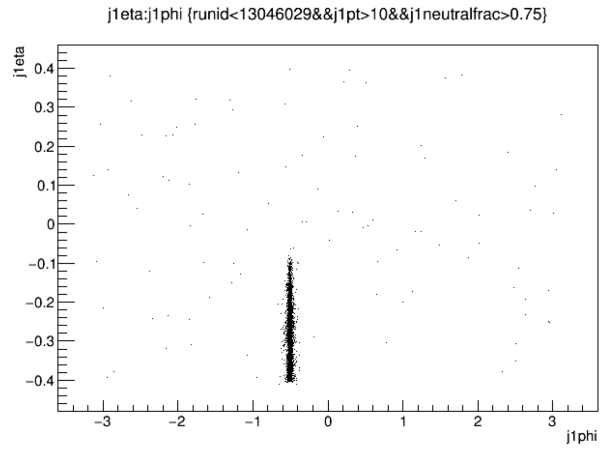


Figure 5: Hot stripe seen in early MB runs. Shown are the jet  $\phi$ - $\eta$  distribution density.

### 3 Jet Reconstructions

Both charged tracks and neutral energies were used to reconstruct jets. Jet reconstruction used anti- $k_T$  algorithm [11] with  $R = 0.6$  with FASTJET 3.1.3. The reconstructed jets were restricted to be inside  $|\eta_{jet}| < 0.4$  so that all tracks/neutral energies of the jets were inside detector acceptance. The jet neutral energy fraction [12] was required to be less than 90% and nonzero to minimize non-collision backgrounds such as beam-gas interactions and cosmic rays. Jets were required to be within  $R = 0.6$  of a triggered jet patch center for calorimeter triggered data [12].

The measured leading jet  $p_T$  distributions for various triggers are shown in Fig. 6.

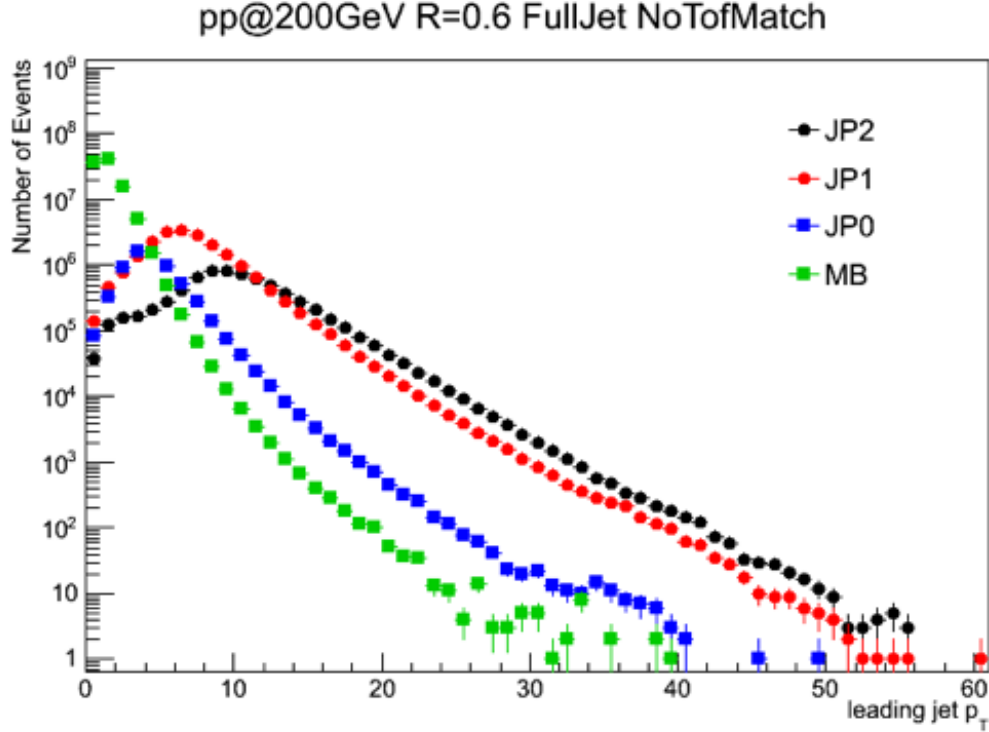


Figure 6: Leading jet  $p_T$  distributions for Jet Patch and Minimum Bias triggers in  $p + p$  collisions at 200 GeV.



## 4 Simulation

The simulation data used in this analysis was PYTHIA Perugia 2012 tune (PYTHIA 6.4.28) with CTEQ6L1 PDF and PARP(90)=0.213 [13, 14]. PYTHIA generated events are processed through GEANT simulation [15]. The GEANT output were further embedded into zerobias experimental measurements. The embedding procedure was to simulate the similar background such as pile up in experimental measurements [16]. This simulation requirement can be found at <https://drupal.star.bnl.gov/STAR/starsimrequests/2015/sep/16/collinsiff-run12>. PYTHIA 6 parameters were tuned through identified particle spectra by Kevin Adkins using STAR published data on PLB 616, 8-16 and PRL 108, 072302. The comparison of tunes for  $\pi^+$  are shown in Fig. 7 from Kevin. The comparison between embedding data and real experiment data can be found at [https://drupal.star.bnl.gov/STAR/system/files/EmbedTrigger\\_v3\\_PDF.pdf](https://drupal.star.bnl.gov/STAR/system/files/EmbedTrigger_v3_PDF.pdf). The default PYTHIA Perugia 2012 without tuning parameters were also used for comparison. PYTHIA 8.215 with default tune (Monash tune) [17] at particle-level were also used. Note: PYTHIA 8 has quite different hadronization than PYTHIA 6. For our simulation, we set the following as stable particles besides pythia default:  $\pi^0$ , pion,  $\eta$ , kaon,  $K^{short}$ ,  $K^{long}$ ,  $\Lambda^0$ ,  $\Sigma^0$ ,  $\Sigma^+$ ,  $\Sigma^-$ ,  $\Xi^0$ ,  $\Xi$ ,  $\Omega$ .

Table 2: Stable particle setting in pythia

---

MDCY (102,1)=0 ! PI0 111
MDCY (106,1)=0 ! PI+ 211
MDCY (109,1)=0 ! ETA 221
MDCY (116,1)=0 ! K+ 321
MDCY (112,1)=0 ! KSHORT 310
MDCY (105,1)=0 ! KLONG 130
MDCY (164,1)=0 ! LAMBDA0 3122
MDCY (167,1)=0 ! SIGMA0 3212
MDCY (162,1)=0 ! SIGMA- 3112
MDCY (169,1)=0 ! SIGMA+ 3222
MDCY (172,1)=0 ! Xi- 3312
MDCY (174,1)=0 ! Xi0 3322
MDCY (176,1)=0 ! OMEGA- 3334

---

Detector-level  $V_z$  distribution in embedding simulation is different than the real data, shown in Figure 8. To account for such difference, we can apply weight in term of  $V_z$  so that they will have the same  $V_z$  distribution. Such procedure has small effect in the final unfolded result, shown in Figures 9 and 10.

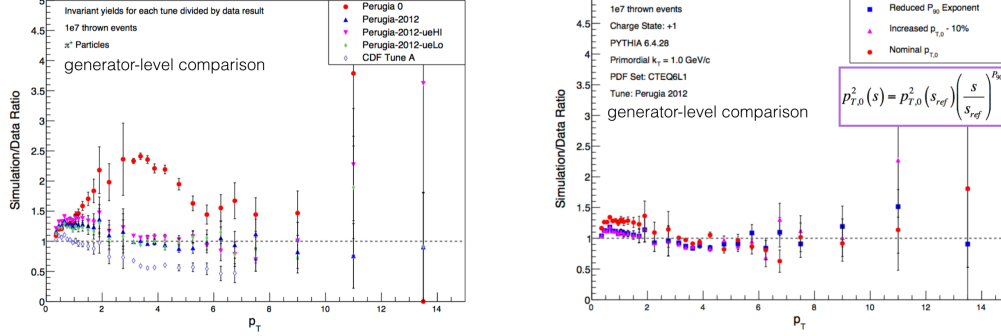


Figure 7: PYTHIA tune comparison for  $\pi^+$   $p_T$  spectra. y-axis is the ratio of simulation and measured data at generator-level.

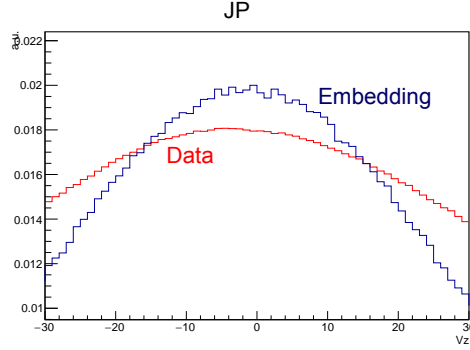


Figure 8:  $V_z$  distribution comparison between real data and embedding detector-level value.

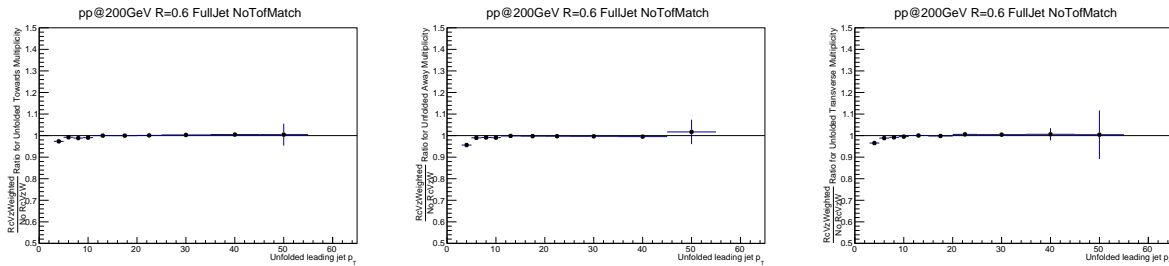


Figure 9: Ratio of unfold charged multiplicity after applying  $V_z$  weight to simulation and without  $V_z$  weight for 3 regions.

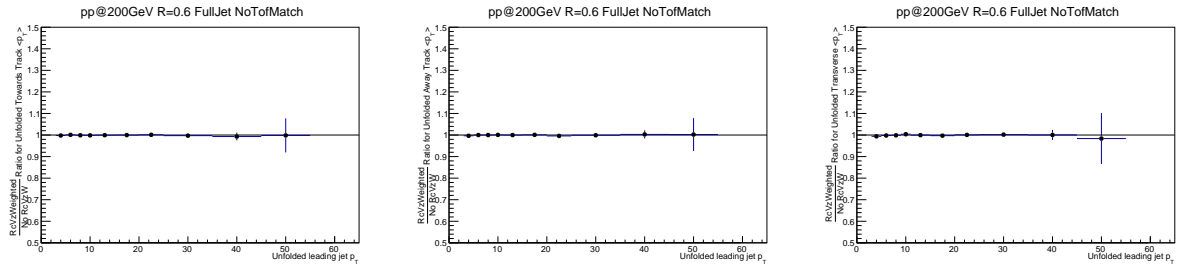


Figure 10: Ratio of unfold charged  $\langle p_T \rangle$  after applying  $V_z$  weight to simulation and without  $V_z$  weight for 3 regions.

## 5 Method

The analysis followed the CDF topological structure method [3]. In each collision event, the leading jet azimuthal angle  $\phi_{jet}$  was defined as reference angle. The charged particles inside this event were categorized into different regions by their azimuthal angle  $\phi_i$  relative to the reference angle  $|\Delta\phi| = |\phi_{jet} - \phi_i|$ , as shown in Fig. 11. Toward region was for particles with  $|\Delta\phi| < 60^\circ$ . Away region was for particles with  $|\Delta\phi - \pi| < 60^\circ$ . Transverse region was for particles with  $60^\circ \leq |\Delta\phi| \leq 120^\circ$ . Underlying-event activity was accessed through the  $\eta$  integrated transverse region. Charged particle multiplicity density  $\frac{N_{ch}}{d\eta d\phi}$  and average particle transverse momentum  $\langle p_T \rangle$  were studied as a function of leading jet  $p_T$ .

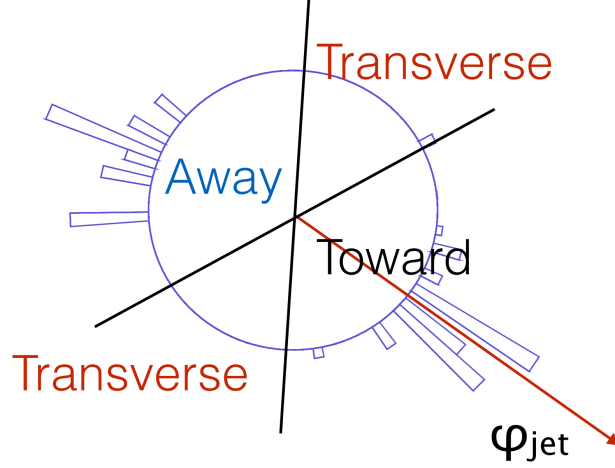


Figure 11: Illustration of topological structure method for underlying event measurement. An event is projected into the collision beam view. Each bar represents a charged particle with its height for  $p_T$  value.  $\phi_{jet}$  denotes the leading jet azimuthal angle.

Figure 12 illustrates particle  $\Delta\phi$  distribution for leading jet  $p_T$  at 10-20 GeV/c in Fig. 12 left panel and leading jet  $p_T$  at 40-50 GeV/c in Fig. 12 right panel.

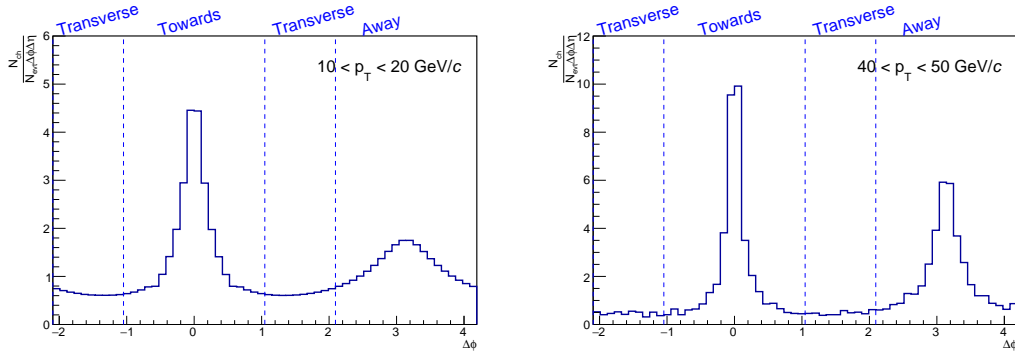


Figure 12: Charged particle  $\Delta\phi$  distribution for leading jet  $p_T$  at (left) 10-20 GeV/c and (right) leading jet  $p_T$  at 40-50 GeV/c.

We also vary the size of transverse region to estimate its effect. Ideally we would like to have the smallest  $\phi$  size to eliminate particles from leading or subleading jets get into the transverse.

However, we also would like to have maximum statistics for transverse region while least leakage from leading or subleading jets. The comparison of  $\Delta\phi = 30^\circ$  and  $\Delta\phi = 60^\circ$  (as default) is shown in Fig. 13. The larger  $\Delta\phi$  size for better statistics was chosen.

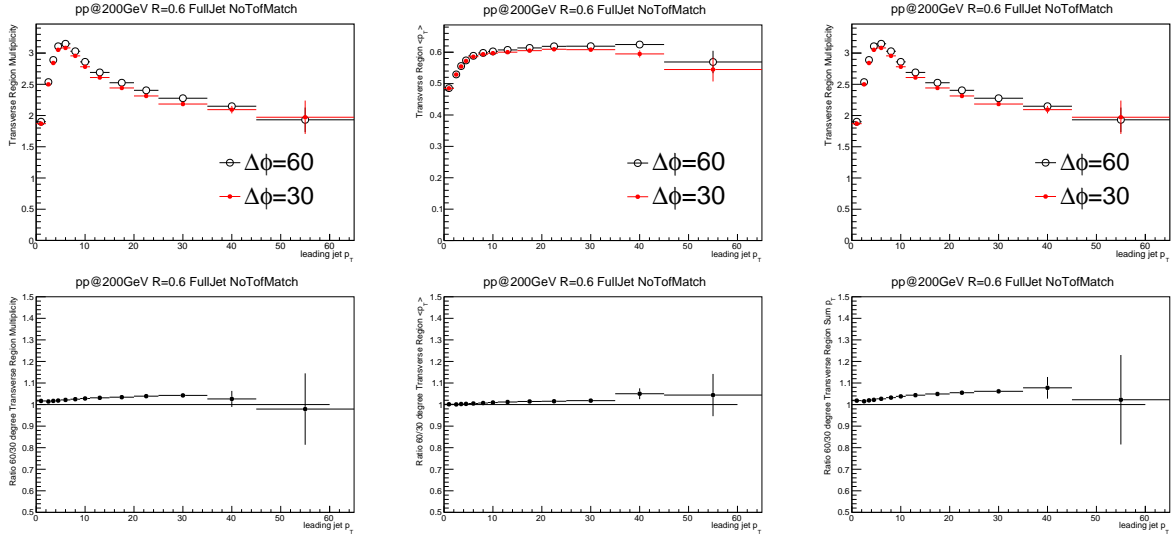


Figure 13: Comparison of transverse region  $\Delta\phi$  size  $30^\circ$  vs  $60^\circ$  for charged multiplicity (left), charged particle average  $\langle p_T \rangle$  (middle) and their sum  $p_T$  (right).  $\Delta\phi = 30^\circ$  of charged multiplicity and sum  $p_T$  are scaled by 2 for comparison. The bottom plots show the ratio of 60 degree and 30 degree for each top plot.

Each event had two transverse regions  $60^\circ \leq \Delta\phi \leq 120^\circ$  and  $-60^\circ \geq \Delta\phi \geq -120^\circ$ . These two transverse regions were further categorized into TransMax and TransMin based on their event activity. The transverse region with higher event activity - either larger charged multiplicity or higher sum  $p_T$  was defined as TransMax, and the other one as TransMin. For most events, the difference between TransMax and TransMin came from statically sampling from same distributions, as symmetrical di-jet production dominates the jet events. MPI and BBR processes are potentially unrelated with hard scattering jet angle and thus likely makes similar contributions to both TransMax and TransMin. ISR/FSR with a wide angle third jet generated could end up in TransMax only. The comparison of TransMax and TransMin are thus sensitive to various underlying-event processes.

## 6 Trigger Bias Correction

The trigger bias correction was done by weighting calorimeter triggered data to have same jet neutral fraction distribution as minimum bias data. Jet neutral fraction ( $R_T$ ) is fraction of neutral constituents (energy deposit in BEMC tower after hadronic corrections) in jet and the jet energy. Figure 14 shows  $R_T$  as a function of leading jet  $p_T$  for MB trigger in black and JP trigger in red. MB  $R_T$  is rather flat in leading jet  $p_T$ . JP  $R_T$  is higher than MB at lower  $p_T$  range less than 20 GeV/c, and then falls and reach an agreement with MB one. For the JP ones, the filled dots are with forward VPD cut ( $|\text{TPC } V_z - \text{VPD } V_z| < 5 \text{ cm}$ ), and the open circles are without VPD cut. As we can see, VPD requirement does not change jet neutral fraction. MB trigger already had a VPD requirement online. But as VPD does not change  $R_T$ , we can use  $R_T$  of MB as if there is not VPD for MB one for reference. The dash curve on the plot is from embedding simulations for MB (without VPD requirement). The embedding simulation can describe MB data.

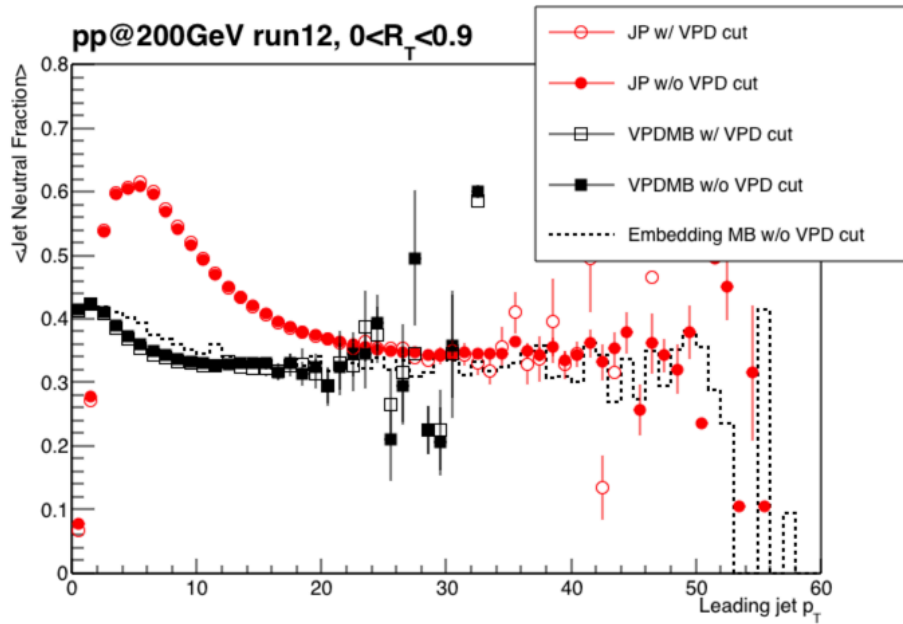


Figure 14: Jet neutral fraction as a function of leading jet  $p_T$  for JP and MB triggers. See text for more descriptions.

The reweighting procedures are as follows: Fill VPDMB and JPs (JP0, JP1, JP2) 2D neutral fraction vs jet  $p_T$  distribution. Both are applied  $|\text{vpd } V_z - \text{TPC } V_z| < 5 \text{ cm}$  cut. The 2D histograms binning in jet  $p_T$ : 0, 2, 3, 4, 5, 7, 9, 11, 15, 20, 100, (no correction applied for jet  $p_T > 20 \text{ GeV}$ ) for neutral fraction are 0-0.9 with 30 binning. 0 and 0.9 are excluded. For each jet  $p_T$  bin, reweigh all JPs 2D histograms (ie,  $\text{TranNtrk}$  vs jet  $p_T$ ) according to the neutral fraction vs  $p_T$  ratio of MB and JPs. After loop finishes, scale the number of events to be same before and after reweighting for each  $p_T$  bin. Note: for jet  $p_T > \text{mbptcut}$ , fill all the bins in MB  $R_T$  histogram to be the same (integrate over  $p_T > \text{mbptcut}$ ). The reason is we want to increase statistics and  $R_T$  distribution

is stable for MB triggers after 5 GeV/ $c$ .

Reweighting for JP with VPD cut are shown in Figures 15 to 17. The corrections are largest for Towards region variables. After the jet neutral fraction reweighting, the ones for JP with VPD cut have the similar shapes and values as the ones in MB with VPD cut. Note, we are not just scale them to be same. Instead, we only reweigh the jet neutral fraction distributions, not the variables themselves. For the Away and Transverse regions, the changes are minimum as expected, since the trigger effect is mostly for leading jet. While, we still see small difference in low  $p_T$  for multiplicities in those regions.

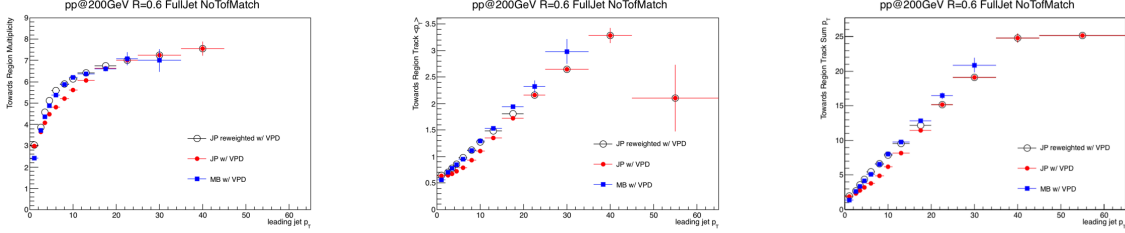


Figure 15: Trigger bias corrections for JP trigger with VPD cut in towards regions for charged TPC tracks: (left) multiplicity, (middle) average  $\langle p_T \rangle$ , sum  $p_T$ . Blue squares are MB with  $|\text{vpd } V_Z\text{-TPC } V_Z| < 5$  cm cut for reference. Red dots are JP with VPD cut. Black circles are reweighted JP with VPD cut.

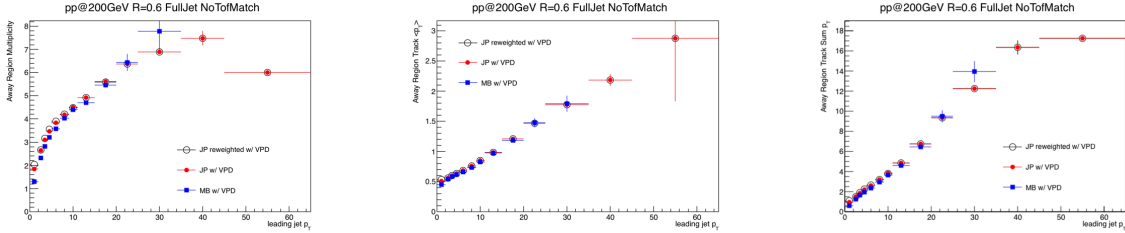


Figure 16: Trigger bias corrections for JP trigger with VPD cut in towards regions for charged TPC tracks: (left) multiplicity, (middle) average  $\langle p_T \rangle$ , sum  $p_T$ . Blue squares are MB with  $|\text{vpd } V_Z\text{-TPC } V_Z| < 5$  cm cut for reference. Red dots are JP with VPD cut. Black circles are reweighted JP with VPD cut.

Next step is to apply correction from MB/JPs with VPD cut to JPs without VPD cut, as we previously discussed VPD cut does not change jet neutral fraction distribution. The results are shown in Figures 18 to 20.

The trigger bias corrections were less than 15% for multiplicity density and less than 20% for  $\langle p_T \rangle$ .

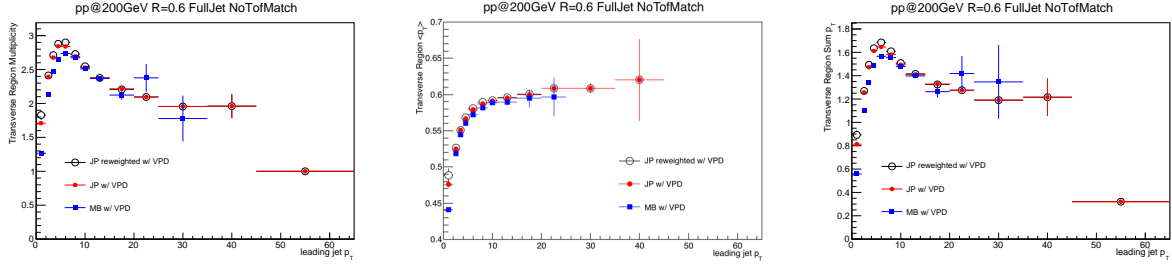


Figure 17: Trigger bias corrections for JP trigger with VPD cut in towards regions for charged TPC tracks: (left) multiplicity, (middle) average  $\langle p_T \rangle$ , sum  $p_T$ . Blue squares are MB with  $|v_{pd} V_z - TPC V_z| < 5$  cm cut for reference. Red dots are JP with VPD cut. Black circles are reweighted JP with VPD cut.

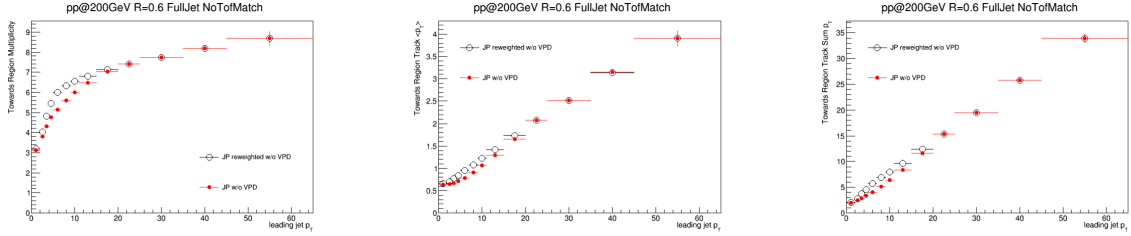


Figure 18: Trigger bias corrections for JP trigger in towards regions for charged TPC tracks: (left) multiplicity, (middle) average  $\langle p_T \rangle$ , sum  $p_T$ . Red dots are JP triggered. Black circles are reweighted JP triggered (the corrected).

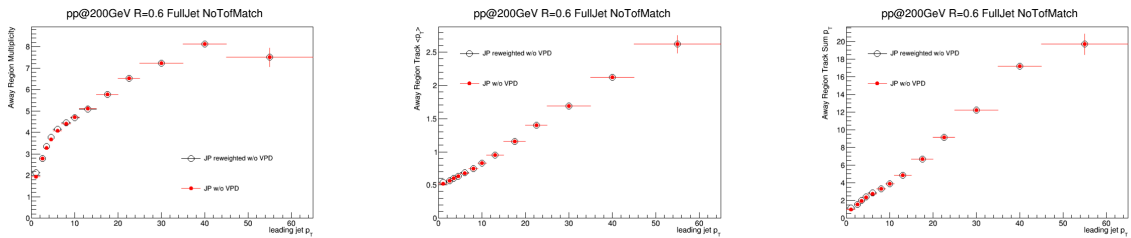


Figure 19: Trigger bias corrections for JP trigger in away regions for charged TPC tracks: (left) multiplicity, (middle) average  $\langle p_T \rangle$ , sum  $p_T$ . Red dots are JP triggered. Black circles are reweighted JP triggered (the corrected).



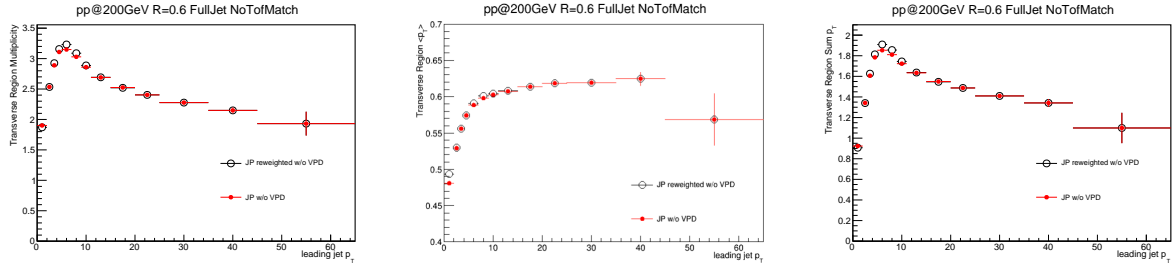


Figure 20: Trigger bias corrections for JP trigger in trans regions for charged TPC tracks: (left) multiplicity, (middle) average  $\langle p_T \rangle$ , sum  $p_T$ . Red dots are JP triggered. Black circles are reweighed JP triggered (the corrected).

## 7 Unfold Detector Effect

The raw measurement data (JPs) after trigger bias correction (see section 6) compared with detector-level simulations (MB) are shown in Figures 21 and 22. Statistical uncertainty only.

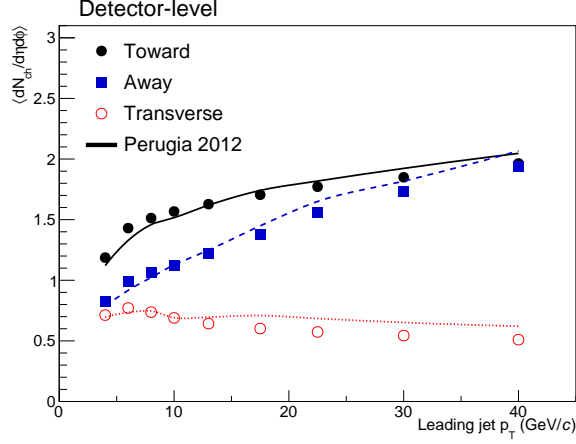


Figure 21: Raw measurement data after trigger bias correction (points) with detector-level simulations (curves) for charged particle multiplicity density vs detector-level leading jet  $p_T$ .

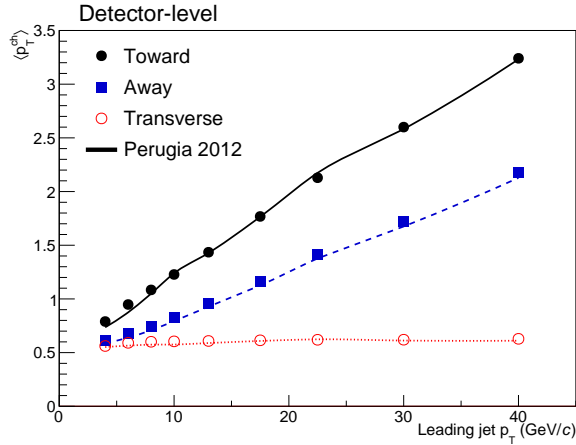


Figure 22: Raw measurement data after trigger bias correction (points) with detector-level simulations (curves) for charged particle  $\langle p_T \rangle$  vs detector-level leading jet  $p_T$ .

The detector inefficiency and background noise corrections were done using 2-dimensional, Bayesian unfolding method <http://hepunx.rl.ac.uk/~adye/software/unfold/RooUnfold.html> [18]. The default setting was iteration=5 and pythia input as prior. The unfolding setting was varied to estimate the systematical uncertainty (Section 10). and The response matrices were constructed from the matches between PYTHIA generator level and GEANT plus zerobias noise reconstructed level observables. A jet pair match was considered to be found if the distance of a leading jet in reconstructed level to a leading jet or sub-leading jet in generator level was less than jet  $R = 0.6$ . When there was a match, the leading jet  $p_T$  in generator level was used for response matrices. For track level observable  $\langle p_T \rangle$ , a track pair match was also required. The

reconstructed level simulation had same track and jet quality requirements as experimental data. The generator level simulation required particle  $p_T > 0.2$  GeV/c,  $|\eta| < 1$  for underlying-event calculation, particle  $p_T > 0.2$  GeV/c for jet reconstruction, and leading jets  $|\eta| < 0.4$ . Figures 23 to 25 shows the projections of 4-dimensional response matrices. The negative bin is intend to show when there is no match found for generator-level and detector-level how the distribution looks like. The simulation data were divided into two subsets to estimate the uncertainty of response matrices to be negligible. The closure test for unfolding can be found in Section 7.2.

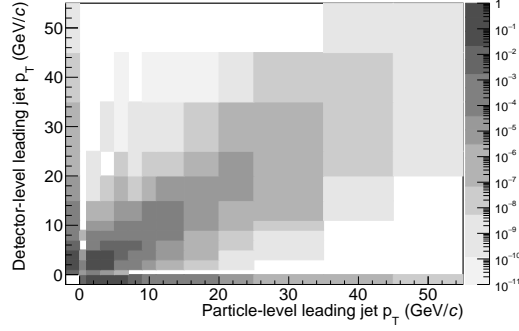


Figure 23: Response matrices for leading jet  $p_T$ .

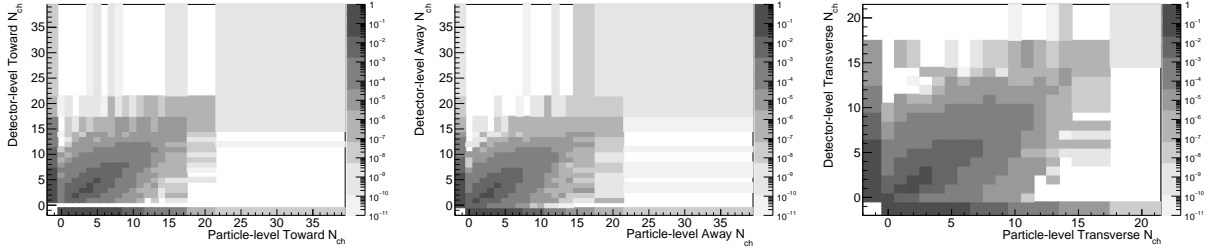


Figure 24: Response matrices of charged multiplicities for (left) Toward region, (middle) Away region and (right) Transverse region.

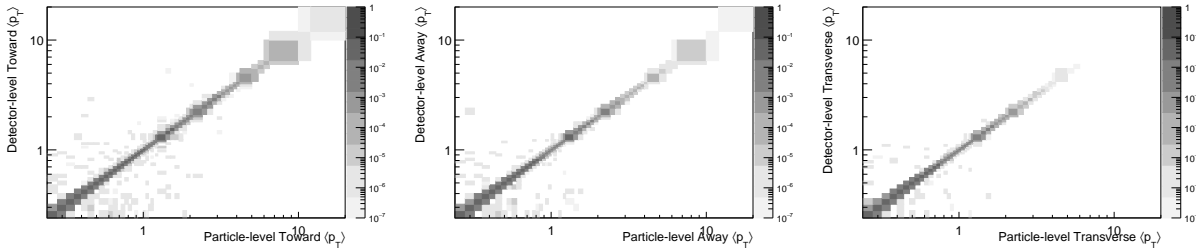


Figure 25: Response matrices of charged particle average  $\langle p_T \rangle$  for (left) Toward region, (middle) Away region and (right) Transverse region.

## 7.1 Unfolded Distributions

Using the unfolding matrix and RooUnfold package, we obtained the unfolded distributions. Here we plot the Transverse region total multiplicity and  $\langle p_T \rangle$  distribution per each jet  $p_T$  bin.

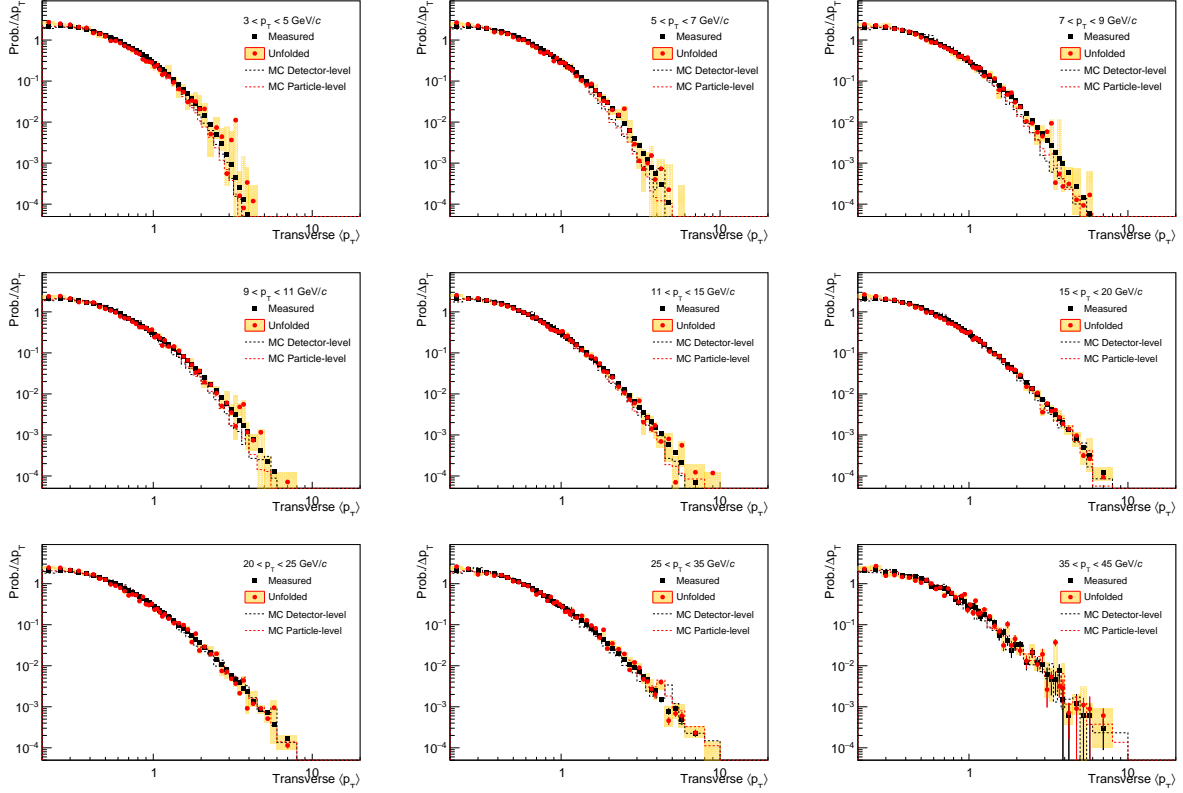


Figure 26: Unfolded and measured Transverse region  $\langle p_T \rangle$  distributions for each jet  $p_T$  bin. Systematical uncertainties are plotted as yellow boxes for unfolded ones. Measured ones are presented with statistical errors only.

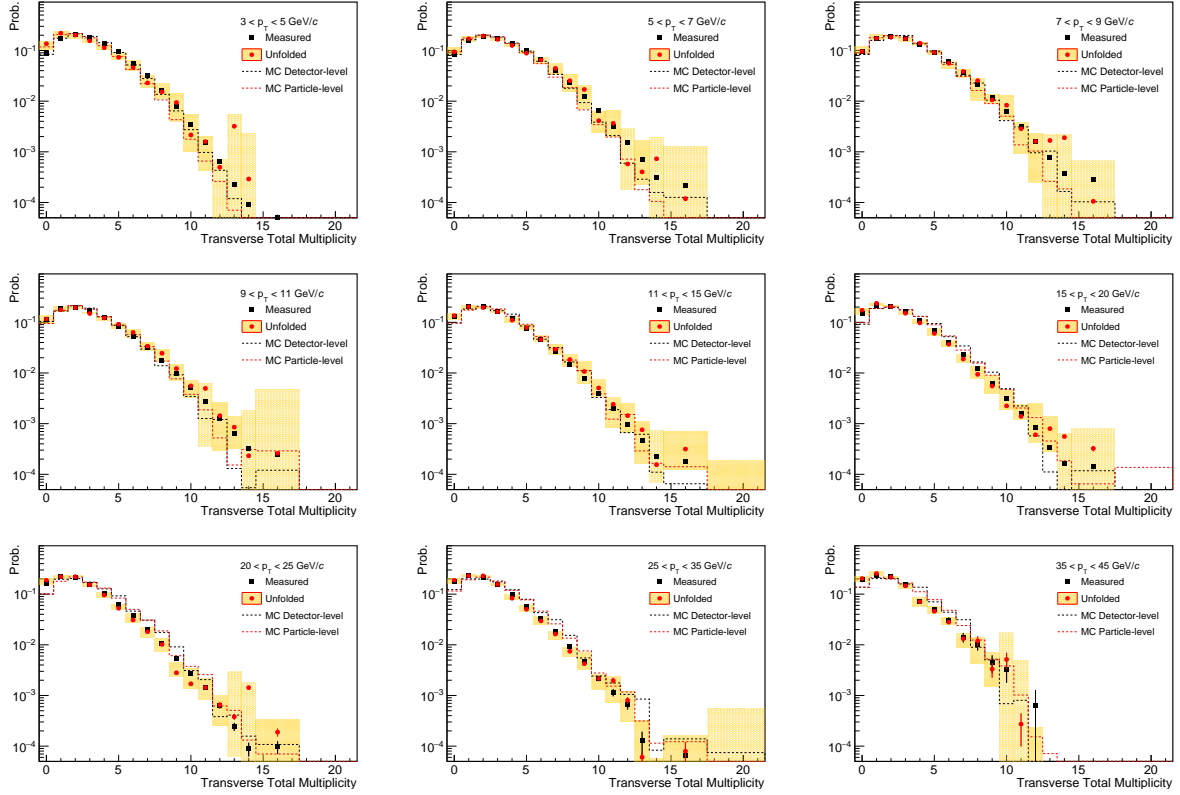


Figure 27: Unfolded and measured Transverse region total multiplicity distributions for each jet  $p_T$  bin. Systematical uncertainties are plotted as yellow boxes for unfolded ones. Measured ones are presented with statistical errors only.

## 7.2 Closure Test

We divide MC data into 2 subsets, use one for training unfolding response matrices, the other for testing. These closure tests are plotted in Figure 28. The unfolded particle-level variables (black lines) are compared to the truth (blue solid lines).

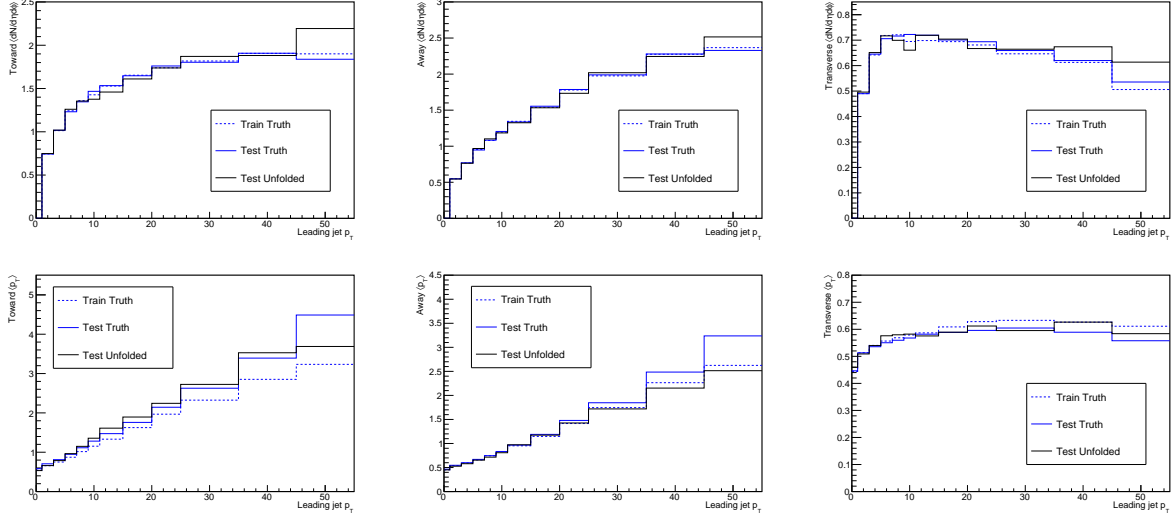


Figure 28: Half MC for training, Half MC for testing. Particle-level charged particle multiplicity density (top) and their  $\langle p_T \rangle$  (bottom) for three regions as a function of particle-level leading jet  $p_T$ . Black lines are unfolded results. Blue solid lines are their truths.

## 8 Pile-up

To minimize pile-up contamination in the measurement, we applied vertex ranking cut, selected the highest ranking primary vertex and required strict  $|dca| < 1$  cm cut on TPC tracks. Additional pile-up could still be presented in the data. In order to correct for those pile-up after event and track quality cuts, we used unfolding to correct for pile-up along with detector effect (Section 7). The pythia output was embedded into zerobias environment which mimicked pile-up in real experiment. Then through the unfolding procedure, we also remove the pile-up effect in the measurement.

## 9 Results

Fully corrected measurements are compared with PYTHIA 6 and PYTHIA 8.

Figure 29 shows the unfolded charged particle multiplicity densities as a function of leading jet  $p_T$ . The transverse region  $\langle N_{ch}/\delta\eta\delta\phi \rangle$ , shown as red dots, increases quickly at lower leading jet  $p_T$ . When jet  $p_T$  reaches 6 GeV/c, transverse  $\langle N_{ch}/\delta\eta\delta\phi \rangle$  starts to saturate and tends to slightly decrease as leading jet  $p_T$  increases further. At LHC energies, mid-rapidity transverse multiplicity were observed to quickly increase and then saturate or slightly increase as leading jet/track  $p_T$  increases [5, 6]. Toward and away region both show a quick rise followed by a slow rise. The tuned and default PYTHIA Perugia 2012, and default PYTHIA 8 Monash simulations are also showed as curves. The tuned PYTHIA Perugia 2012 over-predicts transverse charged multiplicity at  $15 \text{ GeV}/c < \text{jet } p_T < 45 \text{ GeV}/c$  in p+p collisions at 200 GeV, while PYTHIA 6 default one and PYTHIA 8 Monash tune is even higher.

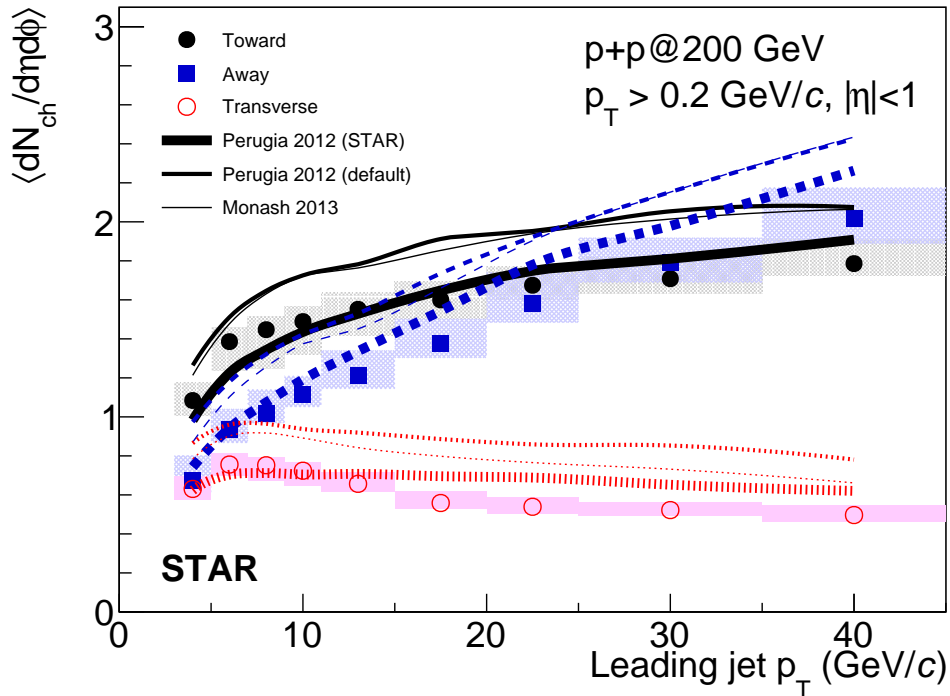


Figure 29: Charged particle density (unfolded) for Toward (black dots), Away (blue square) and Transverse (red dots), compared with tuned PYTHIA generator-level perugia 2012 as wide curves and pythia 8 Monash tune as narrow curves.

Figure 30 shows the unfolded charged particle average  $\langle p_T \rangle$  as a function of leading jet  $p_T$  for three regions. The transverse region  $\langle p_T \rangle$  slightly increases as leading jet  $p_T$  increases. Toward and away region both show linearly increase trends. The simulations, showed as curves, describe the measurements. Figure 31 shows the unfolded charged particle sum  $p_T$  as a function of leading jet  $p_T$  for three regions.



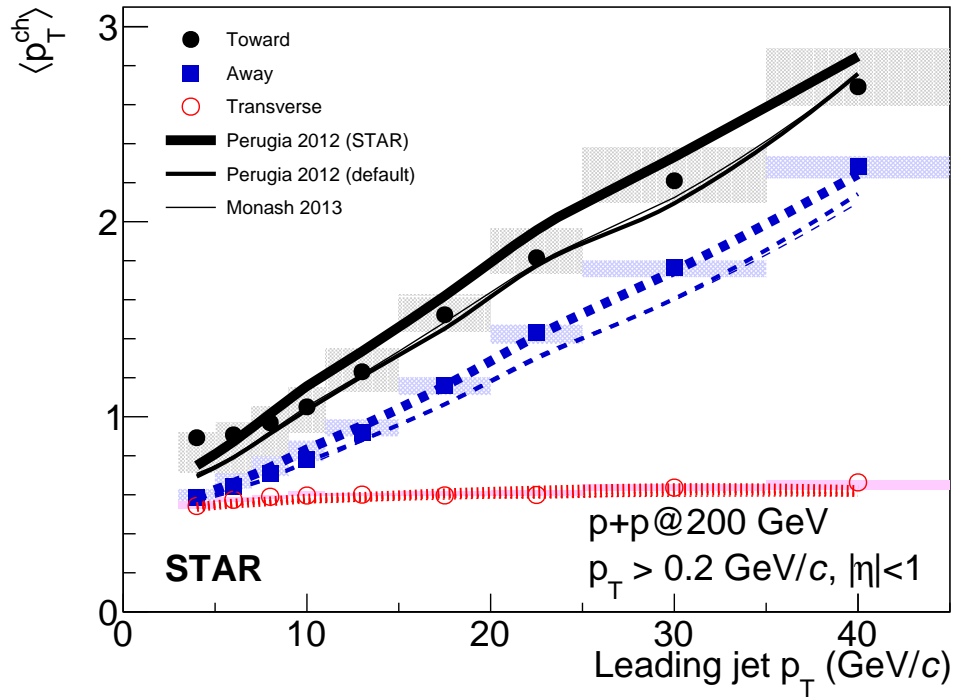


Figure 30: Charged particle average  $\langle p_T \rangle$  (unfolded) for Toward (black dots), Away (blue square) and Transverse (red dots), compared with tuned PYTHIA generator-level perugia 2012 as wide curves and pythia 8 Monash tune as narrow curves.

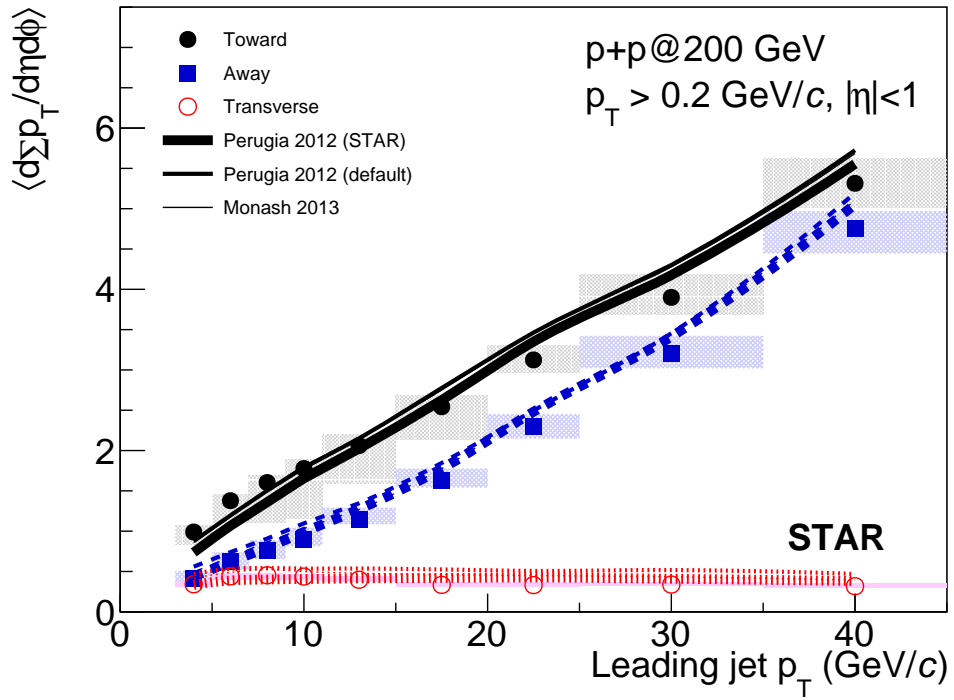


Figure 31: Charged particle sum  $p_T$  (unfolded) for Toward (black dots), Away (blue square) and Transverse (red dots), compared with tuned PYTHIA generator-level perugia 2012 as wide curves and pythia 8 Monash tune as narrow curves.

## 10 Systematical Uncertainty

Systematical uncertainty sources are estimated from unfolding process, TPC tracking efficiency and BEMC tower energy calibration uncertainties. The unfolding method uncertainty was estimated by varying Bayesian iterations, comparing with bin-by-bin unfolding, varying unfolding prior. We change prior when we unfold with different trigger bias correction: when letting GEANT and unfolding to correct for trigger bias without jet neutral fraction weighting, the prior is JP MC distribution; when applying jet neutral fraction weighting, the prior is the \*MB\* (no vpd) MC distribution. The TPC tracking efficiency uncertainty, BEMC tower gain uncertainty and above unfolding uncertainties are added quadratically.

The size of bin for unfolding shall be chosen such that there are enough statistics in each bin and not much bin to bin migration which will cause instability. It is therefore preferred for wider bin. Here we show the comparison between fine binning and wide binning Figures 32 and 33 to check no feature is missed in wide bin.

In order to estimate the uncertainty brought in by unfolding procedure, we varied Bayesian iteration and compared with bin-by-bin unfolding. To estimate the trigger bias correction, we compare the results from trigger bias correction and the ones without this data-driven trigger correction but with embedded trigger simulation (JP0). When changing from MB MC to JP MC, we also effectively change the prior used for the unfolding. Therefore the different prior uncertainties are also taken into account. For reference, we also check the case when just simply scale the measured JP to match measured MB. To combine the systematic uncertainty from those two sources, we analyze data with each combination and take the largest one. Here are more details descriptions on those two parts. For 2-dimensional unfolding, one can use the Bayesian iteration or bin-to-bin correction. The bin-to-bin correction simply multiplies the matrix with ratios, assuming there is no bin to bin migration. For Bayesian iteration, fewer iteration steps means we are not changing too much from initial guess. Too many iteration steps could cause instability in unfolding. After comparing the results from various iteration steps, we chose 5 as default.

The TPC tracking efficiency uncertainty was 5% [19]. For run12 pp200, it was suggested to be 4% during Analysis Meeting Nov. 3rd, 2017. 4% TPC efficiency uncertainty is obtained by Liaoyuan Huo (TAMU MS thesis <http://oaktrust.library.tamu.edu/bitstream/handle/1969.1/ETD-TAMU-2012-05-11173/HUO-THESIS.pdf?sequence=2>). TPC tracking efficiency was added into simulation sample for uncertainty estimation. It is unclear whether this 5% is a relative number or absolute number. To be conservative, we test both cases.

The BEMC calibration systematic uncertainty is done by Kevin Adkins <https://drupal.star.bnl.gov/STAR/theses/phd/kevinadkins>: the uncertainty on the efficiency is 1%, and the uncertainty on the gain calibration is less than 3.8% for run12 pp200 data. We will use 4% as variation on BEMC tower energy to estimate the uncertainty on jet result.

The systematical uncertainties from these two sources are plotted in Figures 34 and 35. The red shadow is unfolding uncertainty. The blue shadow is TPC tracking efficiency uncertainty. The green shadow is BEMC tower gain uncertainty.

The summary is shown in Figures 36 and 37.

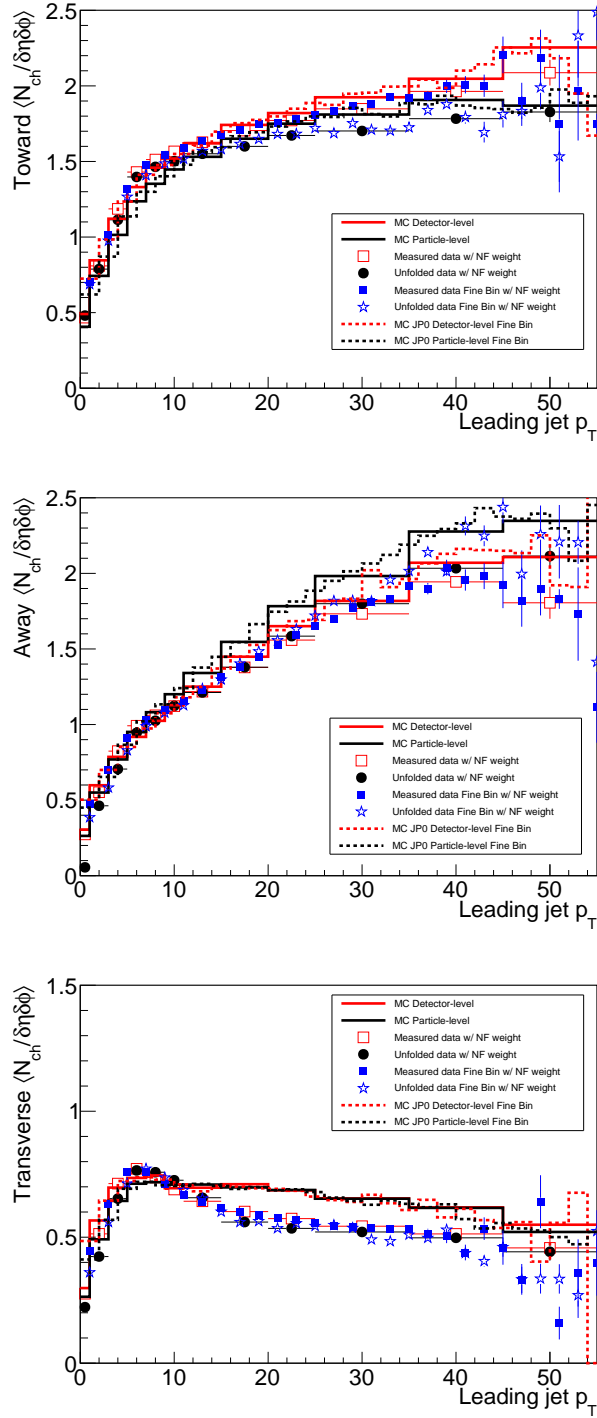


Figure 32: Comparison of fine binning (blue filled squares and open stars) and wide binning (red open squares and black dots) of charged particle density for (top) Toward, (middle) Away and (bottom) Transverse. Jet neutral fraction corrections are applied. Legends with 'Measured' are before unfolding. The unfolded data used Bayesian iteration 5. Embedding data are also shown as histograms.

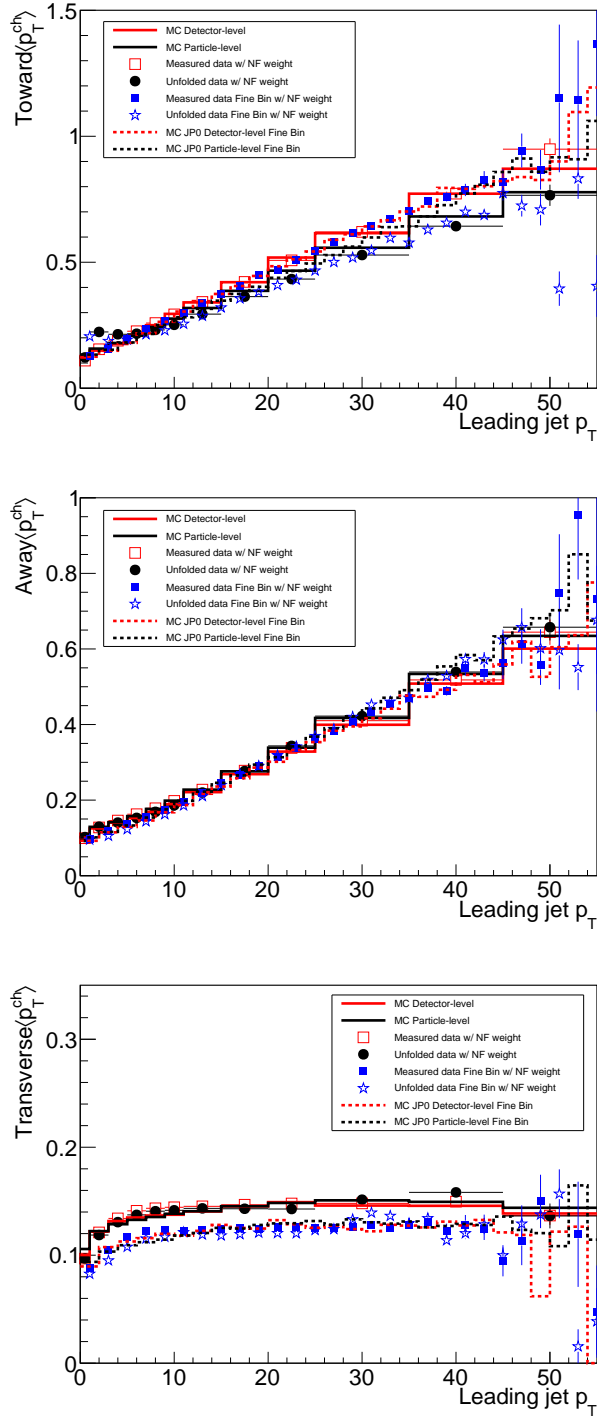


Figure 33: Comparison of fine binning (blue filled squares and open stars) and wide binning (red open squares and black dots) of charged particle average  $\langle p_T \rangle$  for (top) Toward, (middle) Away and (bottom) Transverse. Jet neutral fraction corrections are applied. Legends with 'Measured' are before unfolding. The unfolded data used Bayesian iteration 5. Embedding data are also shown as histograms.

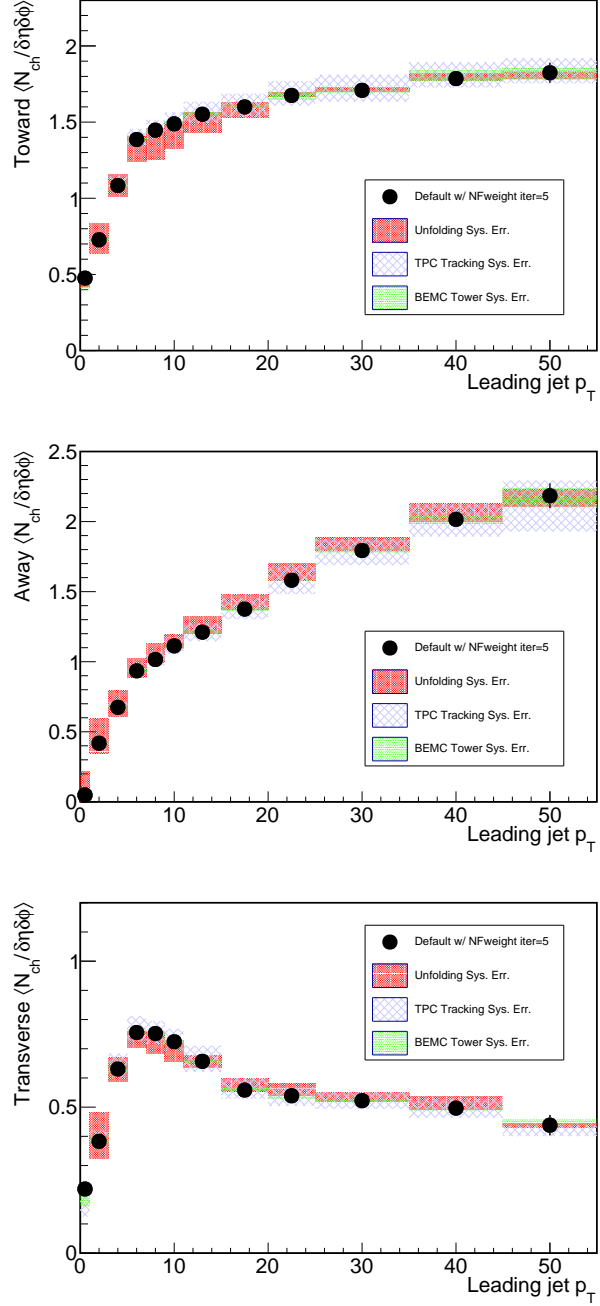


Figure 34: Systematical uncertainties from unfolding and TPC studies of charged particle densities.

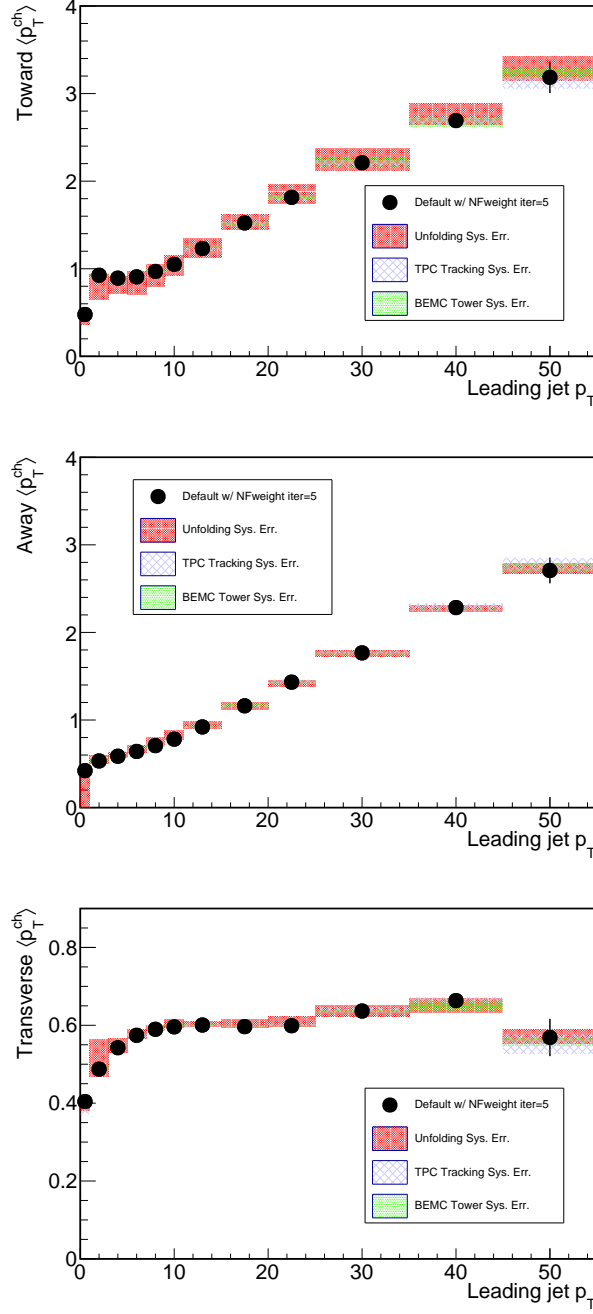


Figure 35: Systematical uncertainties from unfolding and TPC studies of charged particle average  $\langle p_T \rangle$ .

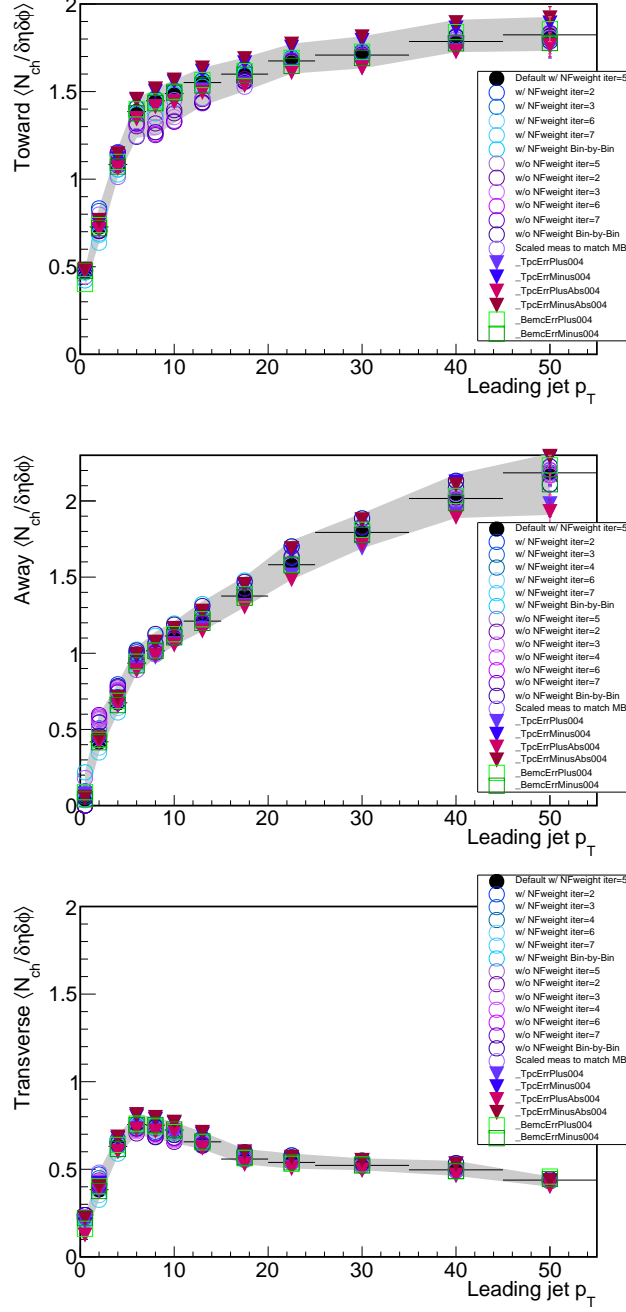


Figure 36: Systematical uncertainty studies of charged particle densities for Toward, Away and Transverse regions.



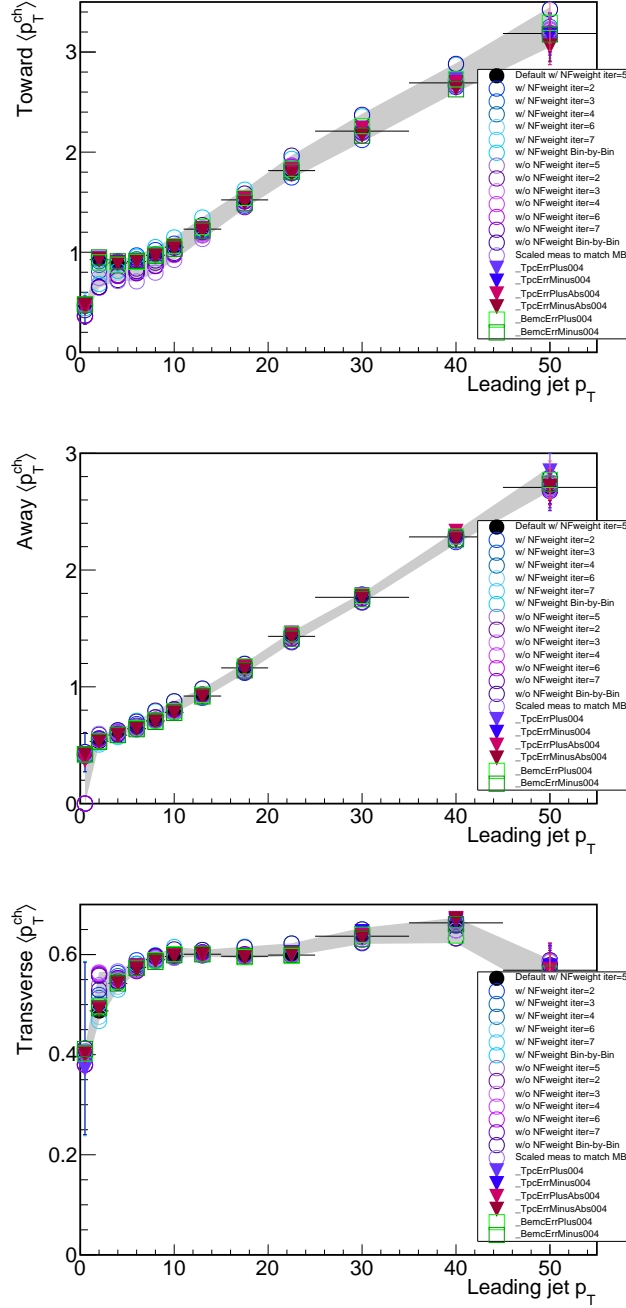


Figure 37: Systematical uncertainty studies of charged particle average  $\langle p_T \rangle$  for Toward, Away and Transverse regions.

# 11 Discussion

## 11.1 TransMax Vs TransMin

Figure 38 shows raw TransMax and TransMin charged particle multiplicity densities as a function of leading jet  $p_T$  at detector-level after trigger bias correction. The difference between TransMax and TransMin is expected to be sensitive to ISR/FSR. At RHIC energy, we observe TransMax and TransMin follows the similar trends. To further investigate the source of their difference, we tested a hypothesis of they come from the same distribution and the only difference is the statistical choice of maximum and minimum. Assuming TransMax and TransMin are both originated from probability density function  $f(x)$ . Then we have TransMax distribution as  $f(max) = 2f(x)F(x)$  and TransMin distribution as  $f(min) = 2f(x)(1 - F(x))$ , while  $F(x)$  is the cumulative distribution function. Using these formula, we calculated the distributions of maximum and minimum from Transverse distribution (average of TransMax and TransMin, shown as curves on Fig. 38) and found they could count for most of the measured data. Any net contribution from additional sources is small. At LHC energies, the different leading jet  $p_T$  dependences were observed for TransMax and TransMin [5, 6]. This difference between RHIC and LHC energies could indicate there is less ISR/FSR at RHIC energy.

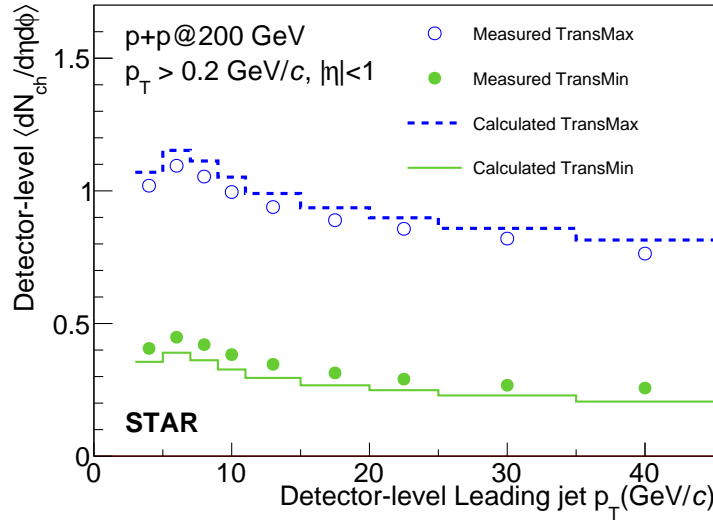


Figure 38: Raw TransMax and TransMin charged particle densities as a function of detector-level reconstructed leading jet  $p_T$ . Curves assume TransMax and TransMin sampled from the same distribution.

## 11.2 Energy Dependence

Underlying-event activities were measured at various collision energies. In order to compare with other experimental measurements which mostly used  $p_T > 0.5$  GeV/ $c$  instead of 0.2 GeV/ $c$ , we also show the results with unfolded only to 0.5 GeV/ $c$  (particle-level) in Fig. 39. The detector-level also used 0.5 GeV/ $c$ . Unfolding maxtrices are also changed. We still used  $|\eta| < 1$ .

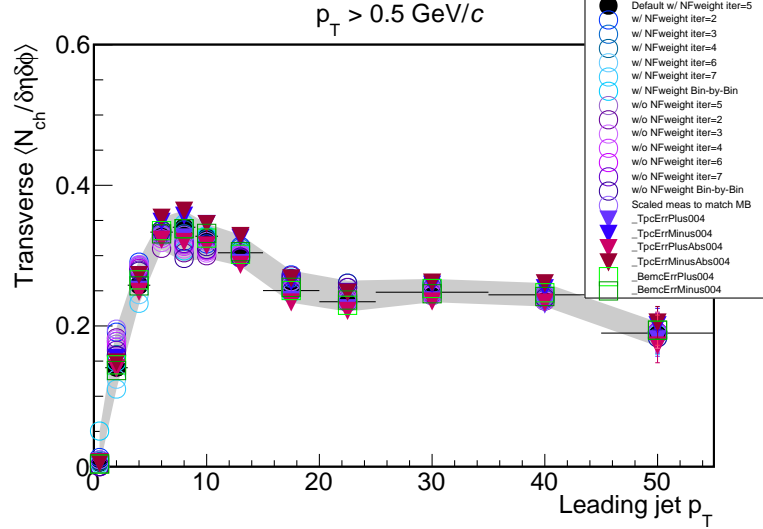


Figure 39: Charged particle density in Transverse region when unfolded to  $p_T > 0.5$  GeV/ $c$  for various unfolding methods, iteration, TPC tracking efficiencies, trigger corrections.

Fig. 40 shows the collision energy dependence. STAR point is from  $20 < p_T^{leading\ jet} < 25$  GeV/ $c$  and charged particle  $p_T > 0.5$  GeV/ $c$ ,  $|\eta| < 1$ . CDF points at 300 GeV, 900 GeV and 1.96 TeV are from leading charged particle  $5 < p_T^{leading\ track} < 6$  GeV/ $c$  and charged particle  $p_T > 0.5$  GeV/ $c$ ,  $|\eta| < 0.8$  [20], at 1.8 TeV are from leading charged jet  $19 < p_T^{leading\ charged\ jet} < 20$  GeV/ $c$  and charged particle  $p_T > 0.5$  GeV/ $c$ ,  $|\eta| < 1$  [21]. ALICE measurements at 900 GeV and 7 TeV are from leading charged particle at  $5 < p_T^{leading\ track} < 6$  GeV/ $c$  and charged particle  $p_T > 0.5$  GeV/ $c$ ,  $|\eta| < 0.8$  [22]. CMS measurement at 2.76 TeV is from leading charged jet at  $17 < p_T^{leading\ charged\ jet} < 22$  GeV/ $c$  and charged particle  $p_T > 0.5$  GeV/ $c$ ,  $|\eta| < 2$  [5]. ATLAS measurements at 900 GeV, 7 TeV and 13 TeV are from leading charged particle  $5 < p_T^{leading\ track} < 5.5$  GeV/ $c$  and charged particle  $p_T > 0.5$  GeV/ $c$ ,  $|\eta| < 2.5$  [23, 6], at 7 TeV is from leading full jet  $20 < p_T^{leading\ jet} < 30$  GeV/ $c$  and charged particle  $p_T > 0.5$  GeV/ $c$ ,  $|\eta| < 2.5$  [24].

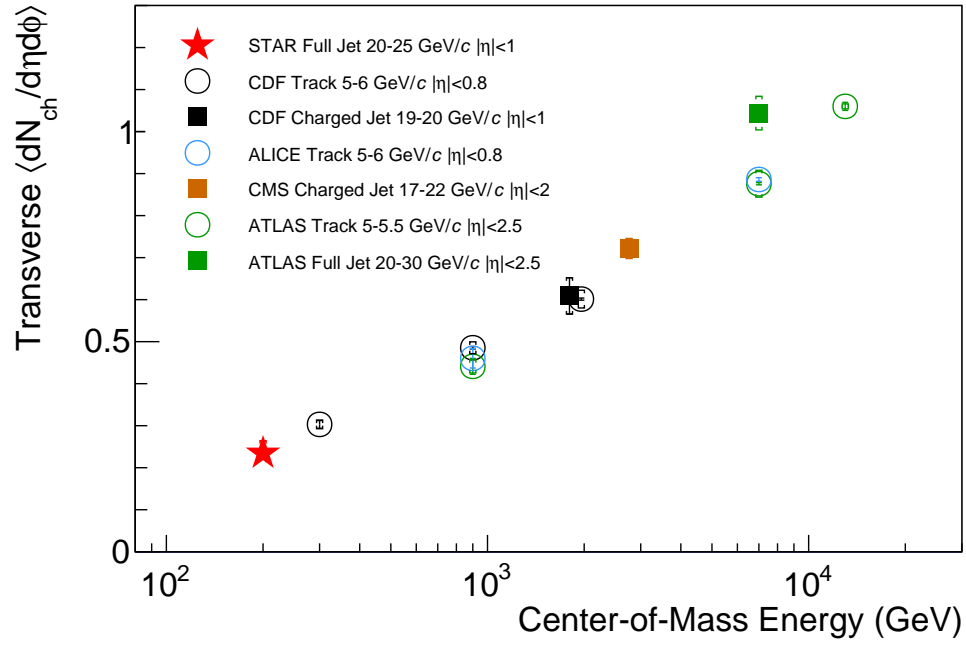


Figure 40: Collision energy dependence of charged particle density in Transverse region.

### 11.3 Leading Charged Particle

One can also use leading charged particle instead of leading jet as hard scattering reference. The difference between leading jet  $\phi$  (when there is a leading jet in the event) and leading charged particle  $\phi$  is shown in Fig. 41. The correlation between leading jet  $p_T$  and leading track  $p_T$  is shown in Fig. 42. The x-axis 0 bin is for events without a jet inside detecting acceptance, which counts for 38% of total events (JP2 trigger).

The transverse charged density and charged particle  $\langle p_T \rangle$  dependence on leading charged particle  $p_T$  are shown in Fig. 43. To eliminate pile-up, we required TOF match for TPC tracks. For y-axis variables, TPC tracking and TOF matching efficiencies are corrected using embedding data. X-axis, leading charged particle  $\langle p_T \rangle$  is the measured detector-level raw value.

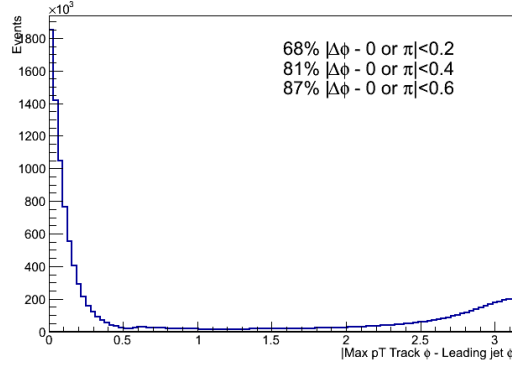


Figure 41:  $\Delta\phi$  difference between leading jet and leading track (both are detector-level raw values.)

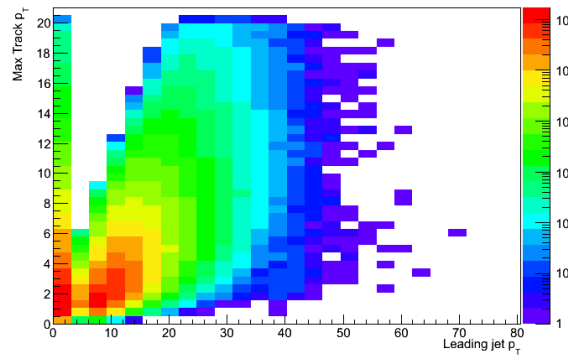


Figure 42: Leading jet  $p_T$  vs leading track  $p_T$  (both are detector-level raw values)

We also show result for  $p_T > 0.5$  GeV/c and  $|\eta| < 1$  case in Fig. 44.

One shall note that for Transverse variables Vs leading charged particle  $\langle p_T \rangle$  results, there is no trigger correction applied, and we do observe there is a difference between triggers.

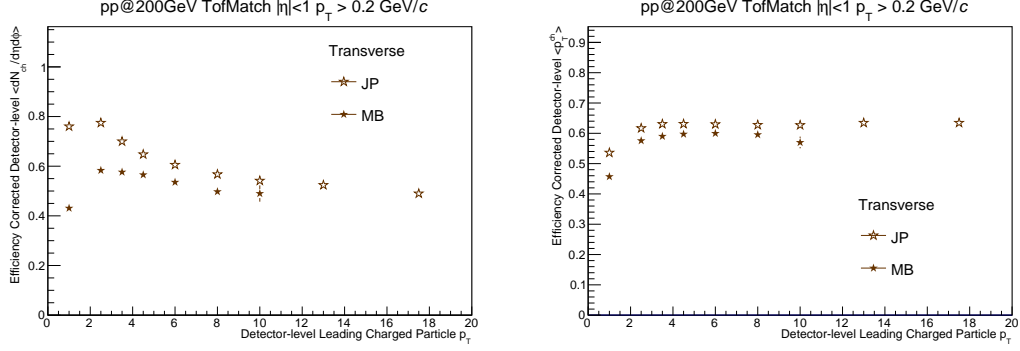


Figure 43: Transverse charged density (left) and charged particle  $\langle p_T \rangle$  (right) dependence on leading charged particle  $p_T$  for VPDMB and JP triggers with  $p_T < 0.2$  GeV/c,  $|\eta| < 1$ . TOF matching is required to eliminate pile-up. The y-axis has TPC tracking and TOF matching efficiencies corrected.

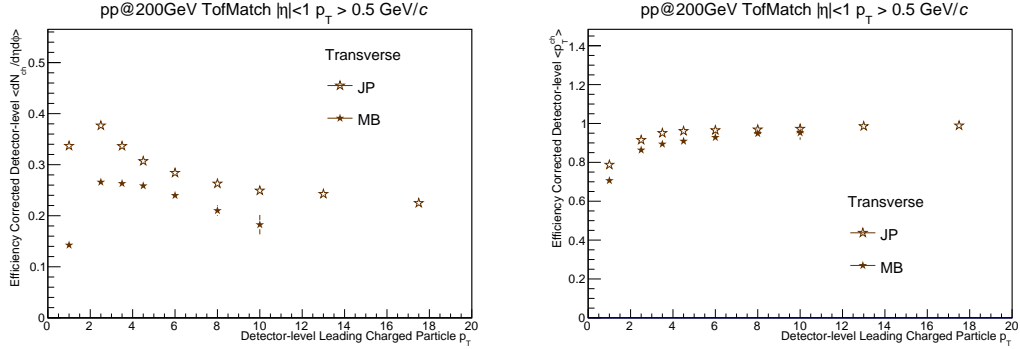


Figure 44: Transverse charged density (left) and charged particle  $\langle p_T \rangle$  (right) dependence on leading charged particle  $p_T$  for VPDMB and JP triggers with  $p_T < 0.5$  GeV/c,  $|\eta| < 1$ . TOF matching is required to eliminate pile-up. The y-axis has TPC tracking and TOF matching efficiencies corrected.

## 11.4 JP0, JP1, JP2

Here we check for the consistence among three JP triggers: JP0, JP1 and JP2. Figure 45 shows the leading jet  $p_T$  distributions after scaled back with average prescale number. At high jet  $p_T > 20$  GeV/ $c$ , the slope among JP triggers are consistent, while MB trigger one has lower number of jet event. Figure 46 shows Transverse Charged Multiplicity (left) and particle average  $\langle p_T \rangle$  (right) as a function of leading jet  $p_T$  for various triggers. For Transverse Charged Multiplicity, JP triggers are consistent with each other, while MB one is lower. For  $\langle p_T \rangle$ , all triggers are consistent.

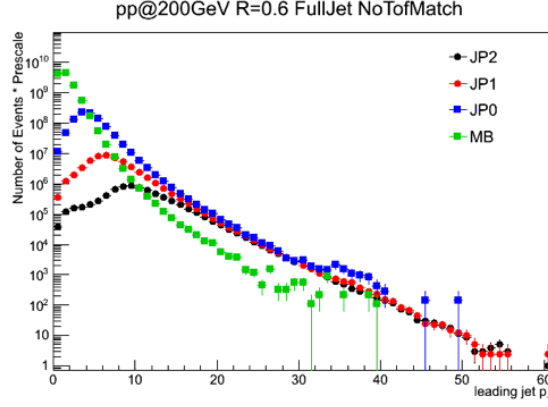


Figure 45: Transverse charged density (left) and charged particle  $\langle p_T \rangle$  (right) dependence on leading charged particle  $p_T$  for VPDMB and JP triggers.

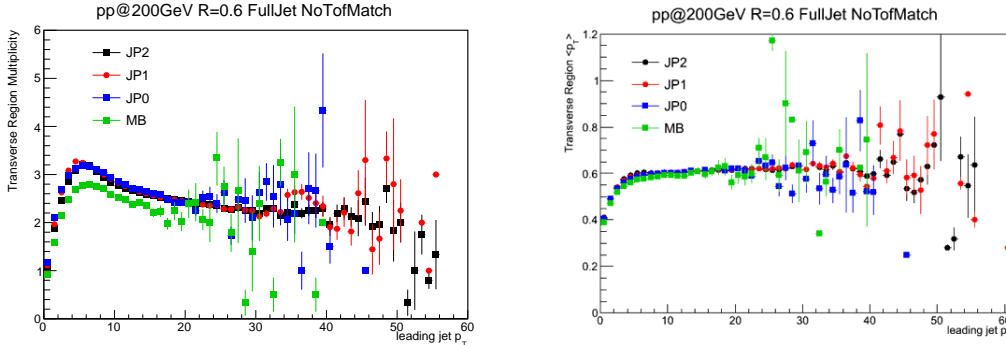


Figure 46: Transverse charged density (left) and charged particle  $\langle p_T \rangle$  (right) dependence on leading charged particle  $p_T$  for VPDMB and JP triggers.

## 11.5 Dijet

The measured Toward and Away regions are different. The difference comes from the selection of leading jet in toward region. The recoil jet may not lie within the detector acceptance. To test such statement, we require the event to have a balanced dijet pair:  $|\phi^{\text{leading jet}} - \phi^{\text{subleading jet}} - \pi| < 0.4$  and  $|p_T^{\text{leading jet}} - p_T^{\text{subleading jet}}|/p_T^{\text{leading jet}} < 5\%$ . The reference  $\phi$  angle still use the leading jet azimuthal angle instead of changing to dijet  $\phi$ . The results are shown in Figure 47. The data with label “Toward”, “Away”, and “Transverse” are detector-level raw measurements from JP triggers without trigger bias corrections. The data with label “Transverse w/ dijet” are from Figures 21 and 22, which are detector-level trigger corrected data without dijet requirement (only leading jet). Compare what we have in Figure 47 with Figures 21 and 22 for “Toward”, “Away”. We can see that the “Toward”, “Away” come together for both multiplicity and  $\langle p_T \rangle$  with dijet selection. While without dijet selection, “Toward”, “Away” are different. Additionally, one can see that with or without dijet, “Transverse” region multiplicity and  $\langle p_T \rangle$  are consistent with each other. The consistence also suggests there is little initial/final state radiation (3-jet events), as suggested by TransMax vs TranMin in Section 11.1.

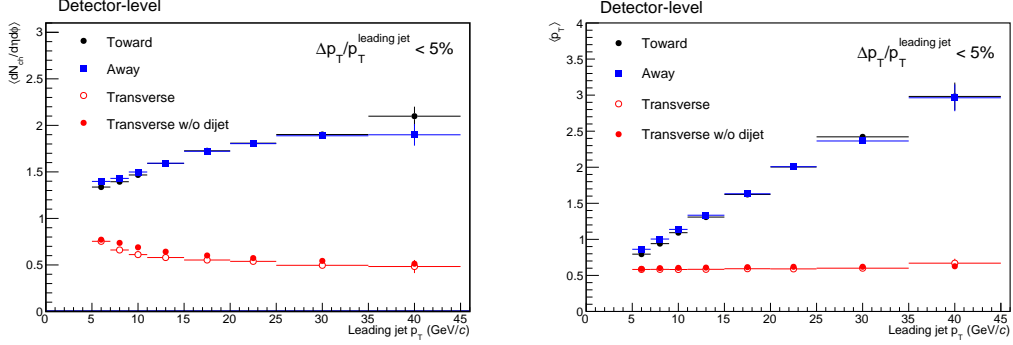


Figure 47: Detector-level charged multiplicity density (left) and charged particle  $\langle p_T \rangle$  (right) dependence on leading charged particle  $p_T$  for dijet and inclusive jet cases.



## 11.6 Unfolding Prior

We used unfolding pythia truth as unfolding prior. For systematical uncertainty estimation, we effectively varies the prior when we change from MB to JP MC for unfolding as in Section 10. In such way, we can estimate the prior change impact as while as ensure the prior is not too far away which may end up wrong local minimal. Therefore it is the preferred way to estimate the prior change impact. However, to demonstrate the prior change works, we also vary prior artificially for test. In this test, we mutliply jet  $p_T$  distribution by  $\exp(-0.1 * p_T)$  as seen in Figure 48. Y-axis is the input prior  $p_T$  distribution for unfolding. The default in red is pythia truth. The mod Prior in black is the modified prior. Note we only change our leading jet  $p_T$  distribution, which rearranges the events and also impact other variables like charged particle multiplicity and  $p_T$ . Now we start 2-D unfolding with modified prior and compare the results with the default one. The comparison are shown in Figures 49 and 50. One can also check the leading jet distribution itself by project 2-D unfolding results onto X-axis of leading jet  $p_T$ . Figure 51 shows the unfolded default divided by the one from modified prior as black points and the prior ratio itself as blue histograms. While on the input level, we give a large change. The output level has much smaller difference (ratio more closer to 1).

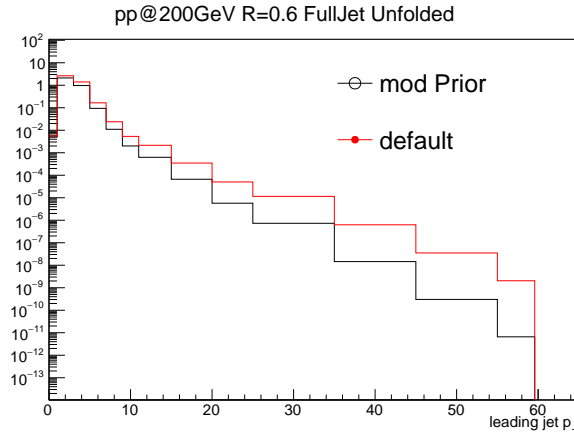


Figure 48: Input prior comparison for the distribution of leading jet  $p_T$ .

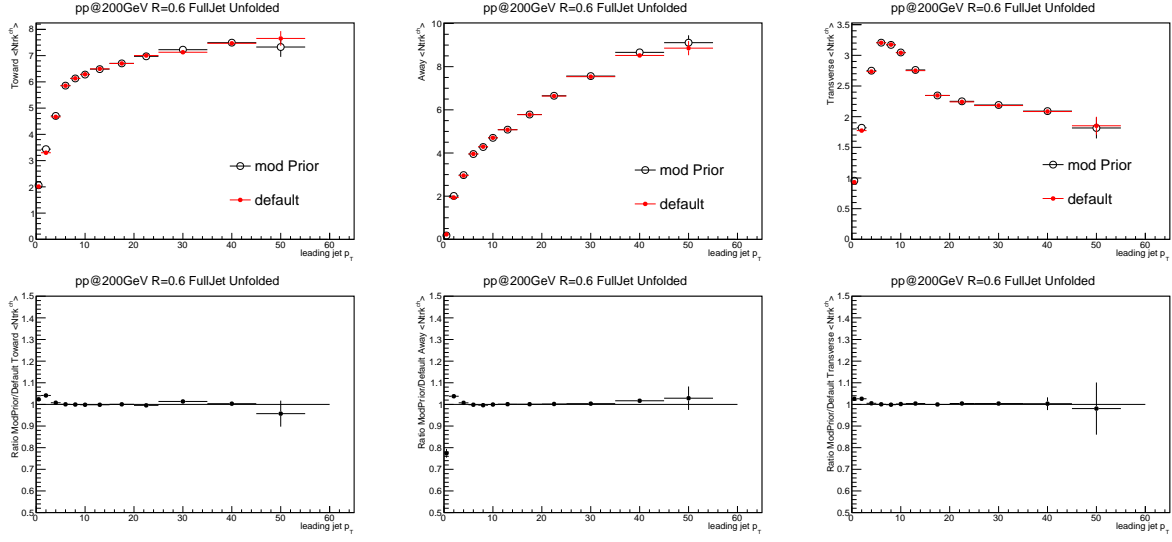


Figure 49: Unfolded comparison for the distribution of charged particle multiplicity in Toward, Away and Transverse region as a function of leading jet  $p_T$ . The bottom plots are the ratios.

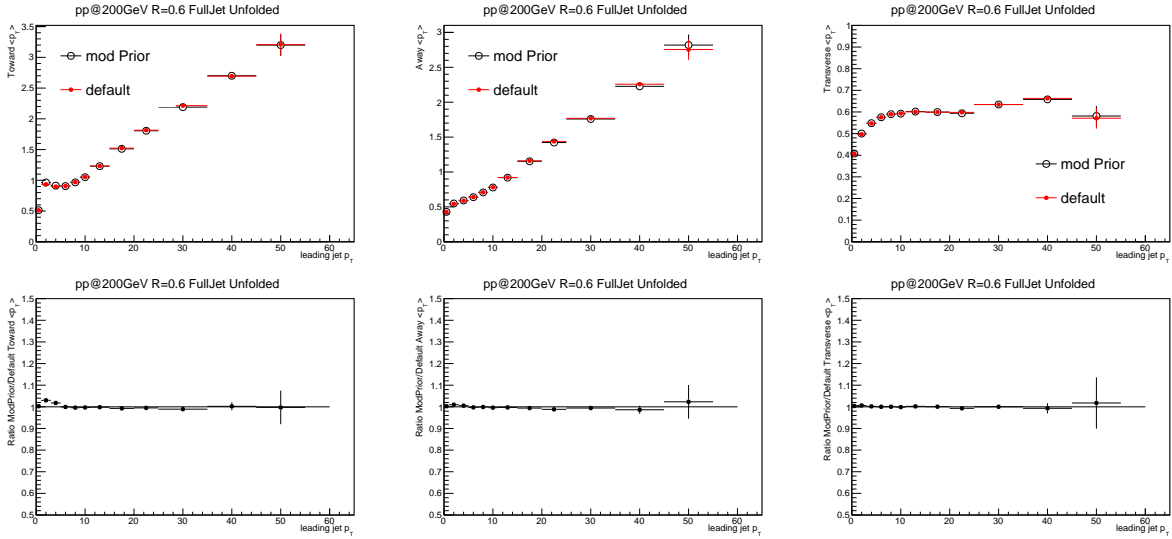


Figure 50: Unfolded comparison for the distribution of charged particle  $\langle p_T \rangle$  in Toward, Away and Transverse region as a function of leading jet  $p_T$ . The bottom plots are the ratios of observables from modified prior divided by that from default.

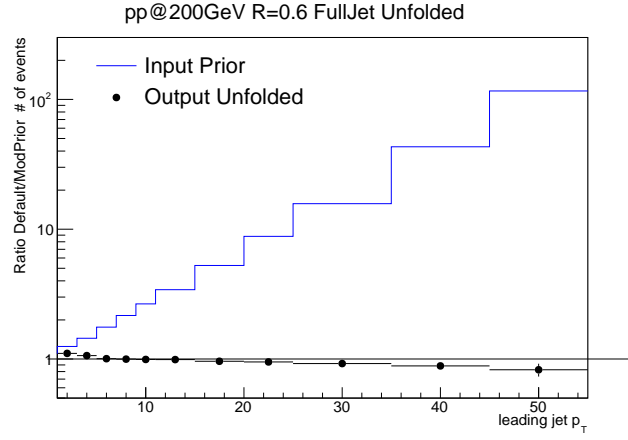


Figure 51: Ratio of default and one from modified prior for the distribution of leading jet  $p_T$ . The blue histogram is input prior ratio. The black points are output unfolded number of events ratio.

## 12 Location of Computing Code

`$CVSROOT/offline/paper/psn0XXX/`

## 13 Conclusion

We reported several observables sensitive to underlying-event activity in p+p collisions at  $\sqrt{s_{\text{NN}}} = 200$  GeV by STAR detector. The results used full jet reconstructed at mid-rapidity  $|\eta_{\text{jet}}| < 0.4$  and  $4 \text{ GeV}/c < p_T < 45 \text{ GeV}/c$ . The charged particle used for underlying-event measurements were for mid-rapidity particles  $|\eta| < 1$  and  $0.2 \text{ GeV}/c < p_T < 20 \text{ GeV}/c$ . The measurement observables were corrected to generator level and can be directly used to compare with theoretical calculation. The detector effect corrections were performed by data-driven trigger correction and embedded full PYTHIA event through GEANT simulations. Uncertainty from the detector effect corrections were included as systematic errors.

The corrected measurement observables used event topological definitions. The particles in the events were defined to be in toward, away, and transverse regions by their azimuthal angles with highest- $p_T$  leading jet. Transverse regions were further splitter as TransMax and TransMin. The charged particle multiplicity densities and their average  $p_T$  in those regions were studied as functions of leading jet  $p_T$ . Their correlations characterized the relationship between underlying-event activity and hard scattering in p+p collisions.

The underlying-event activity results compared with PYTHIA Monte Carlo simulations, combined with minimum bias observables [25, 26] could provide valuable inputs for Monte Carlo modeling.

## References

- [1] Vardan Khachatryan et al. Measurement of the inclusive jet cross section in pp collisions at  $\sqrt{s} = 2.76$  TeV. *The European Physical Journal C*, 76:265, 2016.
- [2] G. Aad et al. Measurement of the jet fragmentation function and transverse profile in proton-proton collisions at a center-of-mass energy of 7 tev with the atlas detector. *The European Physical Journal C*, 71:1795, 2011.
- [3] T. Aaltonen et al. Study of the energy dependence of the underlying event in proton-antiproton collisions. *Physical Review D*, 92:092009, 2015.
- [4] T. Aaltonen et al. Studying the underlying event in drell-yan and high transverse momentum jet production at the tevatron. *Physical Review D*, 82:034001, 2010.
- [5] V. Khachatryan et al. Measurement of the underlying event activity using charged-particle jets in proton-proton collisions at  $\sqrt{s_{\text{NN}}} = 2.76$  tev. *Journal of High Energy Physics*, 09:137, 2015.
- [6] M. Aaboud et al. Measurement of charged-particle distributions sensitive to the underlying event in  $\sqrt{s_{\text{NN}}} = 13$  tev proton-proton collisions with the atlas detector at the lhc. *Journal of High Energy Physics*, 03:157, 2017.
- [7] G. Aad et al. Measurement of distributions sensitive to the underlying event in inclusive z-boson production in pp collisions at  $\sqrt{s_{\text{NN}}} = 7$  tev with the atlas detector. *The European Physical Journal C*, 74:3195, 2014.
- [8] Betty Abelev et al. Underlying event measurements in pp collisions at  $\sqrt{s_{\text{NN}}} = 0.9$  and 7 tev with the alice experiment at the lhc. *Journal of High Energy Physics*, 07:116, 2012.

- [9] S. Chatrchyan et al. Measurement of the underlying event in the drellyan process in proton-proton collisions at  $\sqrt{s_{\text{NN}}} = 7$  tev. *The European Physical Journal C*, 72:2080, 2012.
- [10] S. Chatrchyan et al. Study of the underlying event at forward rapidity in pp collisions at  $\sqrt{s_{\text{NN}}} = 0.9, 2.76$ , and 7tev. *Journal of High Energy Physics*, 04:072, 2013.
- [11] Matteo Cacciari and Gavin P. Salam and Gregory Soyez. The anti- $k_t$  jet clustering algorithm. *Journal of High Energy Physics*, 04:063, 2008.
- [12] L. Adamczyk et al. Precision measurement of the longitudinal double-spin asymmetry for inclusive jet production in polarized proton collisions at  $\sqrt{s_{\text{NN}}} = 200$  gev. *Physical Review Letter*, 115:092002, 2015.
- [13] Peter Zeiler Skands. Tuning monte carlo generators: The perugia tunes. *Physical Review D*, 82:074018, 2010.
- [14] STAR Collaboration. Pythia pp 200gev tune. ?, ?
- [15] S. Agostinelli et al. Geant4a simulation toolkit. *Nuclear Instruments and Methods in Physics Research Section A: Accelerators, Spectrometers, Detectors and Associated Equipment*, 506:250–303, 2003.
- [16] STAR Collaboration. Embedding. ?, ?
- [17] P. Skands, S. Carrazza, and J. Rojo. Tuning pythia 8.1: the monash 2013 tune. *The European Physical Journal C*, 74:3024, 2014.
- [18] Tim Adye. Unfolding algorithms and tests using roounfold. *Proceedings, PHYSTAT 2011 Workshop on Statistical Issues Related to Discovery Claims in Search Experiments and Unfolding, CERN, Geneva, Switzerland 17-20 January 2011*, 2011.
- [19] L. Adamczyk et al. Longitudinal and transverse spin asymmetries for inclusive jet production at mid-rapidity in polarized p+p collisions at  $\sqrt{s_{\text{NN}}} = 200$  gev. *Physical Review D*, 86:032006, 2012.
- [20] T. Aaltonen et al. Pythia pp 200gev tune. *Physical Review D*, 92:092009, 2015.
- [21] T. Affolder and other. Charged jet evolution and the underlying event in  $p\bar{p}$  collisions at 1.8 TeV. *Physical Review D*, 65:092002, 2002.
- [22] Betty Abelev et al. Underlying event measurements in pp collisions at  $\sqrt{s_{\text{NN}}} = 0.9$  and 7 tev with the alice experiment at the lhc. *Journal of High Energy Physics*, 07:116, 2012.
- [23] G. Aad et al. Measurement of underlying event characteristics using charged particles in pp collisions at  $\sqrt{s} = 900\text{GeV}$  and 7 TeV with the ATLAS detector. *Physical Review D*, 83:112001, 2011.
- [24] G. Aad et al. Measurement of the underlying event in jet events from 7 TeV proton-proton collisions with the ATLAS detector. *The European Physical Journal C*, 74:2965, 2014.
- [25] J. Adams et al. Pion, kaon, proton and anti-proton transverse momentum distributions from p+p and d+au collisions at  $\sqrt{s_{\text{NN}}} = 200\text{gev}$ . *Physics Letters B*, 616:8–16, 2005.

- [26] G. Agakishiev et al. Identified hadron compositions in p+p and au+au collisions at high transverse momenta at  $\sqrt{s_{\text{NN}}} = 200\text{gev}$ . *Physical Review Letters*, 108:072302, 2012.